

1 **Electric Fields, Cloud Microphysics, and Reflectivity**
2 **in Anvils of Florida Thunderstorms**
3
4

5
6 J.E. Dye

7 National Center for Atmospheric Research, Boulder CO
8

9 M.G. Bateman

10 Universities Space Research Association, Huntsville AL
11

12 H.J. Christian

13 Univ. of Alabama in Huntsville, Huntsville AL
14

15 E. Defer

16 Observatoire de Paris, Paris, France
17

18 C.A. Grainger

19 Univ. of North Dakota, Grand Forks ND
20

21 W.D. Hall

22 National Center for Atmospheric Research, Boulder CO
23

24 E.P. Krider

25 Univ. of Arizona, Tucson AZ
26

27 S.A. Lewis

28 NOAA/Univ. of Colorado, Coop. Inst. for Research in Environmental Sciences, Boulder CO
29

30 D.M. Mach

31 Univ. of Alabama in Huntsville, Huntsville AL
32

33 F.J. Merceret

34 National Aeronautics and Space Administration, Kennedy Space Center FL
35

36 J.C. Willett

37 Garrett Park MD
38

39 P.T. Willis

40 NOAA Cooperative Institute for Marine and Atmospheric Sciences; Miami FL
41
42

43 Submitted to J. of Geophysical Research May 23, 2006

44 Revised November 5, 2006
45

46
47 Corresponding Author: James Dye

48 dye@ucar.edu; Cell phone: 720-530-5012; FAX: 303-497-8171

49 NCAR; PO Box 3000, Boulder CO 80307-3000

50 EXPRESS Mail: 3450 Mitchell Lane, FL3; Boulder CO 80307-3000
51

51 ABSTRACT

52 A coordinated aircraft - radar project that investigated the electric fields, cloud
53 microphysics and radar reflectivity of thunderstorm anvils near Kennedy Space Center is
54 described. Measurements from two cases illustrate the extensive nature of the
55 microphysics and electric field observations. As the aircraft flew from the edges of anvils
56 into the interior, electric fields very frequently increased abruptly from ~ 1 to >10 kV m^{-1}
57 even though the particle concentrations and radar reflectivity increased smoothly. The
58 abrupt increase in field usually occurred when the aircraft entered regions with a
59 reflectivity of 10 to 15 dBZ. It is suggested that the abrupt increase in electric field may
60 be because the charge advection from the storm core did not occur across the entire
61 breadth of the anvil and was not constant in time. Screening layers were not detected near
62 the edges of the anvils. Some long-lived anvils showed subsequent enhancement of
63 electric field and reflectivity and growth of particles, which if localized, might be a factor
64 in explaining the abrupt change of field in some cases.

65 Comparisons of electric field magnitude with particle concentration or reflectivity
66 for a combined data set that included all anvil measurements showed a threshold
67 behavior. When the average reflectivity, such as in a 3-km cube, was less than
68 approximately 5 dBZ, the electric field magnitude was <3 kV m^{-1} . Based on these
69 findings, the Volume Averaged Height Integrated Radar Reflectivity (VAHIRR) is now
70 being used by NASA, the Air Force and Federal Aviation Administration in new
71 Lightning Launch Commit Criteria as a diagnostic for high electric fields in anvils.

72

72 1. Introduction

73 Numerous studies have been conducted to examine the microphysical conditions
74 and radar reflectivity structure of convective clouds when charge separation is beginning
75 and electric fields are intensifying, but few studies have examined the decay of electric
76 fields in space and/or time in thunderstorm anvils as a function of the cloud microphysics
77 and radar reflectivity. Since thunderstorm anvils can contain high electric fields, they
78 pose a significant threat for triggering lightning during space flight operations. Until
79 recently the mission launch rules at the National Aeronautics and Space Administration
80 (NASA) Kennedy Space Center (KSC) and the Air Force Eastern Range would prevent a
81 space vehicle from flying through non-transparent anvils or even an anvil detached from
82 the parent convection if lightning had occurred within the last 3 hours in the parent storm
83 or the anvil [Krider et. al., 1999].

84 The Airborne Field Mill II experiment (ABFM II) was conducted near KSC to
85 measure the electric field, reflectivity and microphysics in thunderstorm anvils (and other
86 clouds) produced by deep convection with the hope that the launch constraints involving
87 anvil clouds could be safely relaxed. In this paper we present a brief overview of the
88 ABFM II campaigns, examples of some of the measurements, and a synthesis of the
89 results obtained in 14 different flights through anvils. During the analysis of ABFM II
90 observations and while attempting to compare the observations with estimates of electric
91 field decay predicted from a simple model [Willett and Dye, 2003], we found that
92 reflectivity and strong electric fields persisted and became uniform in a stratiform-like
93 mid-level layer for many tens of minutes over many tens of kilometers well downstream
94 of the parent convection. This “enhancement” of reflectivity, electric field and

95 microphysics in two long-lived anvils is discussed in a separate paper [Dye and Willett,
96 2006] that argues that weak updrafts were probably present and that charge separation
97 must have occurred in these long-lived anvils. The simple model based on ABFM II
98 particle observations, which was used to estimate the electric field decay in passive anvils
99 and compared with the electric field observations from ABFM II, will be described
100 elsewhere.

101

102 2. The Airborne Field Mill Experiment

103 The ABFM II campaigns were conducted during June 2000 and May-June 2001 to
104 investigate the relationships between microphysics, radar reflectivity and the decay of
105 electric fields (both spatially and temporally) in thunderstorm anvils and other clouds. In-
106 situ measurements of the 3-D electric field; particle concentration, types and sizes; and
107 standard thermodynamic and flight measurements were made using a Citation II jet
108 aircraft operated by the University of North Dakota (UND). [See Ward et al., 2003, for
109 information on the Citation and its instrumentation for ABFM II.] The aircraft
110 measurements were coordinated with reflectivity measurements by the WSR-74C radar at
111 Patrick Air Force Base, FL and the NEXRAD WSR-88D radar at Melbourne, FL. The
112 occurrence and location of intra-cloud (IC) and cloud-to-ground (CG) lightning flashes
113 were determined using the KSC Lightning Detection and Ranging (LDAR) system
114 [Lennon and Maier, 1991] and the KSC Cloud to Ground Lightning Surveillance System
115 (CGLSS) [Maier, 1991].

116 The anvils ranged in size from small anvils of short-lived airmass thunderstorms to
117 anvils formed by mid-level outflow to large anvils of intense multi-cellular, long-lived

118 thunderstorms. Initial penetrations were often made across the anvil outflow close to the
119 convective cores of the storms. Subsequent cross anvil passes were made at different
120 distances downstream to examine the decay of the electric field both with time and
121 distance. Some passes were also made along the axis of the anvil outflow either towards
122 or away from the core of the storm.

123 Aircraft penetrations were typically made at altitudes ranging from 7 to 11 km MSL
124 [-15 to -45 C], with 80% of the penetrations made at 8 to 10 km MSL (about -20 to -35
125 °C) and mostly near 9 km MSL (~-31 to -32 °C), because the middle of the anvil was
126 usually at these altitudes. (Hereafter all altitudes are referenced to mean sea level, MSL).
127 Spiral ascents or descents were made through the anvils when Air Traffic Control (ATC)
128 would allow, but these were relatively infrequent due to heavy airliner traffic in that
129 region of Florida. In some cases the aircraft arrived after most of the electric field had
130 already decayed but these cases are also useful because we know the reflectivity history
131 of these storms and the time of the last lightning relative to the aircraft penetrations.
132 Decisions on where to fly were based on interactions between the air crew and ground
133 coordinators at the Air Force Range Operations Control Center (ROCC), where aircraft
134 track could be overlaid on vertical and horizontal cross-sections of the radar reflectivity
135 and where displays of lightning, ground-based electric field, and satellite observations
136 were available in real time.

137 In the following sub-sections we present a brief summary of instruments and
138 measurement systems used during the project. More information on each of these
139 measurement systems can be found in Dye et al. [2004].

140

141 2.1 Airborne Measurement of Electric Field

142 The 3-dimensional electric field was measured in situ from the UND Citation using
143 6 low noise, high dynamic range, rotating-vane field mills that were designed and built at
144 NASA Marshall Space Flight Center [Bateman et al., 2006]. The use of two input
145 channels with overlapping gains and 16 bit analog-to-digital converters permitted a
146 measurement range from less than 1 V/m to 150 kV m⁻¹. The data were digitized inside
147 each field mill close to the source so as to minimize electrical noise from the aircraft. The
148 mills were time synchronized to within 16 ms of each other by a central data collection
149 computer for the field mills and the overall timing accuracy was within 50 ms of UTC.
150 The data were recorded at 50 samples s⁻¹ but for this paper were averaged and plotted at 1
151 sample s⁻¹.

152 When the aircraft was out of cloud, the charge on the aircraft was usually very
153 small. Based on the analysis of Mach and Koshak [2003] we feel that the uncertainty in
154 the measured electric field out of cloud was within +/- 10%. When the aircraft penetrated
155 a cloud, however, the errors increased significantly due to aircraft charging. In this case,
156 E_z and E_y, the field components in the vertical and along the wings, respectively, were
157 accurate to about 20%. The E_x component along the fuselage was much less accurate.
158 (We used a right-handed coordinate system with E_z positive upward, E_x positive forward
159 and a sign convention in the traditional physics sense, i.e. a positive field shows the
160 direction in which a positive charge would move. E_x, E_y and E_z are relative to the
161 aircraft.) More details on the placement of the field mills on the aircraft, the techniques
162 used to determine the 3-dimensional electric field and calibration of the system can be
163 found in Mach and Koshak [2003] and in Appendix B of Dye et al., [2004].

164

165 2.2 Airborne Microphysical Measurements

166 Five separate microphysical instruments were flown on the Citation to determine
167 the concentration, sizes, and types of particles ranging from a few microns to about 5
168 centimeters, thus covering a range from frozen cloud droplets to large aggregates.
169 Descriptions of all instruments used are available in the literature. Herein we cite only
170 recent publications that discuss the measurement techniques, sources of measurement
171 error and that include references to earlier published studies of that instrument. A Particle
172 Measuring Systems (PMS) Forward Scattering Spectrometer Probe (FSSP) was used for
173 the size range of a few microns to $\sim 50 \mu\text{m}$. The FSSP was designed to measure water
174 droplets and has shortcomings in ice and mixed phase clouds [Field *et al.*, 2004]. We
175 used the FSSP only as an indication of the relative concentration of the small ice
176 particles. A PMS 2D Cloud probe (2D-C) [Strapp *et al.*, 2001; Field *et al.*, 2006]
177 nominally covered the range of $30 \mu\text{m}$ to a few millimeters and gave shadow images of
178 the particles from which information on particle type can be obtained as well as the size
179 and concentration. A PMS 1D cloud probe (1D-C), which is similar to the 2D-C but does
180 not image the particles, gave measurements of the concentration of particles in 15 size
181 bins from 15 to $960 \mu\text{m}$. A Stratton Park Engineering Corp (SPEC) Cloud Particle Imager
182 (CPI) [Lawson *et al.*, 2001] provided images of particles with resolution of $2.5 \mu\text{m}$ over
183 its effective size range of $\sim 10 \mu\text{m}$ to about 1 mm, with images of the larger sizes limited
184 by the small sample volume. Measurements from the CPI were used only to examine
185 particle type. The SPEC High Volume Particle Sensor (HVPS) [Lawson *et al.*, 1998]
186 images particles in the nominal range of 1 mm to 5 cm with a resolution of $400 \mu\text{m}$ along

187 the direction of flight and 200 μm in the cross stream direction. Like the 2D-C, special
188 software is needed to process the data and determine concentration in different size
189 ranges. We used software developed at NCAR for processing and displaying the ABFM
190 II microphysical measurements. In general the cloud physics instruments worked well
191 and normally there was very good agreement in the overlap regions between different
192 probes.

193 Assigning an uncertainty to the concentration and size measurements from each
194 instrument is not straightforward. The concentration, n_i , in any size interval, i , measured
195 by these instruments is C_i/v_i , where C_i and v_i are the number of counts and sample
196 volume in that size interval. The statistical uncertainty of the measured concentration in
197 that size bin is then approximately $(\sqrt{C_i})/v_i$. The number of counts in the size bins of each
198 instrument is dependent upon the integration time and the relative abundance of particles.
199 In ABFM II for 10 s averaging periods, in the small/intermediate-sized intervals we
200 typically counted many tens or hundreds of particles, whereas for the larger size bins of
201 each instrument the number of counts was typically only a few particles. Thus there is
202 little statistical uncertainty (<10%) for the small to mid size range measured by each
203 instrument and a factor of 2 or more uncertainty for the largest sizes. Because of the
204 overlap between the 2D-C and the HVPS for the millimeter-sized particles, the statistical
205 uncertainty of the composite size distributions in this overlap region is probably <30%,
206 when both instruments are functioning well. Errors in sizing for these instruments are
207 greatest when the particle size becomes comparable to the spacing between the diode
208 elements [See Strapp et al., 2001] and when the particles are larger than or near the size
209 of the full width of the diode array. For the 2D-C flown on the Citation this width is

210 roughly 1 mm. In the middle of the size range of each instrument, sizing errors are
211 probably <15%.

212 In addition to the particle probes the Citation carried a King liquid water sensor and
213 a Rosemount Icing Detector [Heymsfield and Miloshevich, 1989]. The measurements
214 from the King liquid water sensor were rarely used in our ABFM II analyses because we
215 flew mostly in anvils and other cloud regions that contained primarily ice particles. The
216 Icing Detector was a valuable instrument that allowed us to determine when supercooled
217 liquid water was present in our clouds. Analysis of the icing detector measurements by
218 Schild [2003] and other unpublished undergraduate work at UND showed no evidence of
219 supercooled water in the ABFM II anvils, so all particles discussed in this paper are
220 considered to be ice.

221

222 2.3 Radar Reflectivity Measurements

223 Radar measurements were obtained from a WSR-74C (74C) radar located at Patrick
224 Air Force Base (about 25 km south of KSC) and the WSR-88D (88D) NEXRAD radar
225 located at Melbourne, Florida about 18 km to the southwest of the 74C radar. (The
226 location of the 74C radar was used as the origin in all of our radar plots). The 74C radar
227 provides support for all launch operations at KSC and the Air Force Eastern Range. The
228 74C is a C-band (5.3 cm), horizontally polarized weather radar without Doppler
229 capability. The peak power was 250 kW with a pulse repetition frequency (PRF) of 160
230 Hz. The beam width was 1.05 degrees and the pulse width was 4 μ s. It had a maximum
231 range of 256 km with a range resolution of 250 m. Measurements were made during

232 antenna ascent and descent with twelve interleaved 360 degree sweeps. A complete
233 volume scan was made every 2.5 min.

234 The NEXRAD 88D is an S-band 10 cm circularly polarized, Doppler weather radar.
235 The beam width was 0.95 degrees; the pulse width was 1.57 or 4.7 μ s; and peak power
236 was 750 kW. The PRF varied from 318 to 1304 Hz. Pulse pair processing was used to
237 recover the Doppler information. The normal range was 230 km, but degraded reflectivity
238 data could be obtained at ranges as far as 460 km. A complete volume scan took 5 to 6
239 min. All ABFM II measurements were from the Volume Coverage Pattern precipitation-
240 mode scan strategy, VCP 11 [OFCM, 2003].

241 The universal format data from both radars were converted to a Cartesian 1 km grid
242 with 1 km horizontal and vertical spacing over a 225 by 225 km domain using SPRINT
243 [Mohr et al., 1986]. SPRINT was configured to perform a bi-linear interpolation with a
244 maximum acceptable distance of 0.2 km to relocate a closest point estimate and with no
245 range interpolation. The reflectivity was converted from dB to a linear scale for
246 interpolation. Subjective comparisons of horizontal and vertical cross-sections of the 74C
247 and 88D data sets showed good agreement when attenuation of the 74C was not a factor.
248 Additionally, statistical tests were done for a limited set of quantitative reflectivity
249 comparisons and found that the systematic differences (without attenuation) were less
250 than 1 dBZ when examined over volumes of several tens of km^3 .

251 Attenuation of the 74C measured reflectivity was apparent behind regions of heavy
252 precipitation or when the radome of the 74C was wetted due to precipitation. The 74C
253 observations were manually checked for each flight to determine times when attenuation
254 had occurred. For the analyses presented in Section 4 below NEXRAD data were

255 substituted for the 74C data when 74C attenuation occurred for an individual case. Both
256 radars have a cone of silence directly above the radar that was not scanned because it lies
257 at an elevation angle higher than the elevation of the highest sweep angle. At an anvil
258 altitude of 9 km, this corresponded to a horizontal diameter of ~20 km for the 74C and
259 ~30 km for the 88D radars. The airborne data set which is used in Section 4 were
260 carefully edited so that it did not include data points when the anvil was in the cone of
261 silence of the appropriate radar.

262 When the difference between adjacent elevation sweeps exceeded the beam width
263 of that radar, scan gaps occurred, i.e. the radar did not completely sample the entire
264 volume of radar space. These gaps produced a ragged appearance of the anvil tops, bases
265 and sides in the cross sectional displays of the reflectivity measurements, particularly for
266 storms far from the radar. The effects of radar propagation can also cause the actual
267 altitude to differ from the indicated altitude by a couple of kilometers [Wheeler, 1997].
268 These issues could present a problem when trying to compare the airborne measurements
269 with the radar reflectivity measurements from the 1x1x1 km gridded data.. Some of the
270 grid points can be in a scan gap and there can also be propagation effects. Constant
271 Altitude Plan Position Indicator (CAPPI) plots and vertical sections along the aircraft
272 tracks that are presented in this paper were based on the 1-km gridded radar data, so they
273 sometimes display the artifacts. However, when airborne measurements of electric field
274 or particle concentrations are plotted versus the radar reflectivity in Section 4 below, the
275 1 km gridded reflectivity data were averaged in dBZ over a 3-km cube in order to
276 mitigate the effects of scan gaps and propagation effects. Pixels with no detectable return

277 were not included in the averages and we required that 16 of the 27 pixels in a 3-km cube
278 contain measurable reflectivity.

279

280 2.4 Lightning Measurements

281 Two lightning detection systems were used during ABFM II to determine
282 occurrence, location, and frequency of lightning discharges. The Lightning Detection and
283 Ranging (LDAR) system, which is a total lightning system using time-of-arrival
284 techniques, located the sources of VHF radiation from lightning from 63 to 69 MHz
285 [Lennon and Maier, 1991]. It consisted of a central site and 6 remote sensors that were
286 approximately 10 km radius from the central site. Studies by Boccippio et al., [2000a and
287 b] show that the flash detection efficiency is >90% within 100 km range and <25% at 200
288 km range. The VHF source location error distribution is a function of range with a mean
289 horizontal error of about 200 m at 100 km. [See Figure 3 in Boccippio 2000b]. For most
290 of our analyses we plotted the individual VHF sources overlaid on radar CAPPIs to show
291 when and where lightning discharges occurred and have not separated the sources into
292 flashes.

293 The Cloud to Ground Lightning Surveillance System (CGLSS) provided the
294 locations and times of cloud-to-ground (CG) return strokes [Maier, 1991]. During ABFM
295 II this system used 6 Global Atmospheric Inc. 141-T Advanced Lightning Direction-
296 Finders operating over a wide bandwidth in and below the MF, an IMPACT 280-T
297 Advanced Position Analyzer employing both radio-direction-finding and time-of-arrival
298 techniques, and associated displays. The system was similar to the National Lightning
299 Detection Network [Cummins et al., 1998]. The sensors extended approximately 40 km

300 to the north, west and south of KSC. Within the perimeter of the network the accuracy of
301 location of CG strokes was about 300 m [Boyd et al., 2005]. At a range of 100 km from
302 the network the accuracy degraded to roughly 3 km. When all six sensors were
303 functioning properly the detection efficiency was better than 98%. More information on
304 LDAR and CGLSS use in ABFM II can be found in Appendices F and G of Dye et al.,
305 [2004].

306

307 3. Examples from Two Storms

308 One of our first observations during ABFM II was that the transition from weak
309 electric fields ($\sim 1 \text{ kV m}^{-1}$) to thunderstorm strength fields ($\sim 10 \text{ kV m}^{-1}$) in anvils was
310 usually quite abrupt, and it occurred when the Citation flew from regions that had a
311 reflectivity $< 10 \text{ dBZ}$ into regions with greater reflectivity. Analysis also showed that the
312 transition to strong fields was quite rapid in comparison to the more smoothly varying
313 particle concentrations in all size ranges and radar reflectivity. Based on this finding by
314 June 2001 the ground coordinators could often tell the aircraft crew where to expect large
315 increases/decreases in electric fields based on the reflectivity display. In this section we
316 present two cases that illustrate the kinds and quality of the observations that were made
317 during ABFM II and that also illustrate the abrupt increases in electric field.

318

319 3.1 13 June 2000

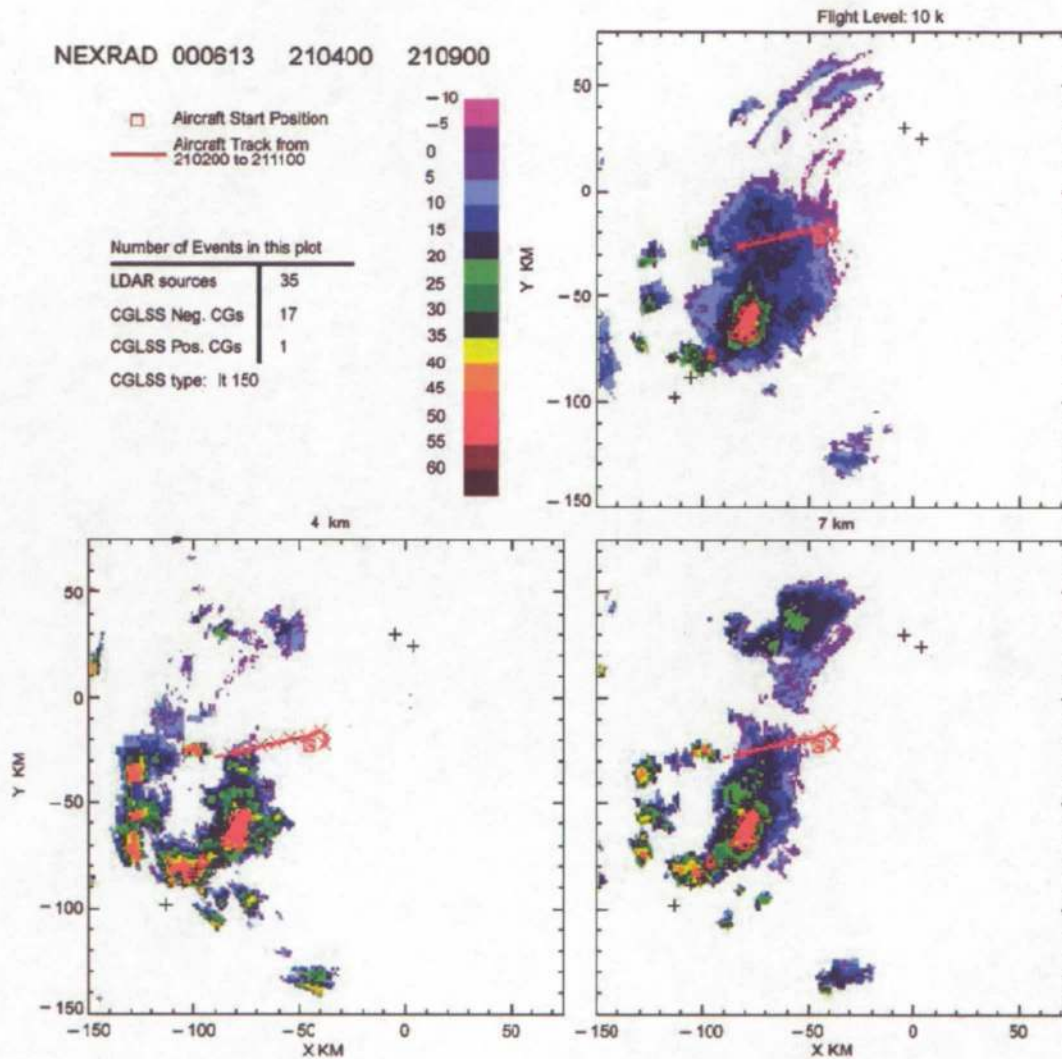
320 The June 13th storm was a long-lived storm with a well developed anvil that was
321 investigated by the Citation for over 3 hours from 2045 UTC to after 2400 UTC. (UTC is
322 used throughout this paper; subtract four hours for local daylight time.) The Citation first

323 entered the anvil when it was relatively small (~40 km length at 10 km altitude), but well
324 defined. By 2200 the anvil at 10 km altitude, as deduced from radar observations,
325 extended more than 100 km downwind of the original convective core. Penetrations were
326 made from east to west or vice versa at 10 to 11 km altitude across the anvil at 25 to 50
327 km from the storm core from 2050 until 2225. After 2225 penetrations were made along
328 or opposed to the direction of the wind along the axis of the anvil from southwest to
329 northeast until ~0005, first at 11km altitude, then 9 km and finally 8 km as the anvil
330 subsided. In a separate paper Dye and Willett [2006] use this case as well as the case of 4
331 June 2001 to illustrate the enhancement in reflectivity and electric field that was observed
332 in some long-lived anvils. More information on the latter stages of the June 13th storm
333 can be found in that paper.

334 An example of an early cross anvil penetration from 2103 to 2111 is shown in
335 Figure 1, as the Citation was climbing from 10 to 11 km. The reflectivity structure in the
336 10 km CAPPI reflects the downshear outflow and some upshear divergence from the
337 upper level updraft. The maximum reflectivity in the storm at this time was 55 – 60, 50 –
338 55, and 40 to 45 dBZ at 4, 7 and 10 km, respectively but the reflectivity pattern of the
339 core is obscured in Figure 1 by the red triangles showing the CG strokes. The CGLSS
340 system showed that CG lightning occurred in the convective cores from 1915 until 2135.
341 Because the LDAR system was not functioning properly in June 2000 until the following
342 day, there is a paucity and miss-location of LDAR VHF sources in Figure 1.

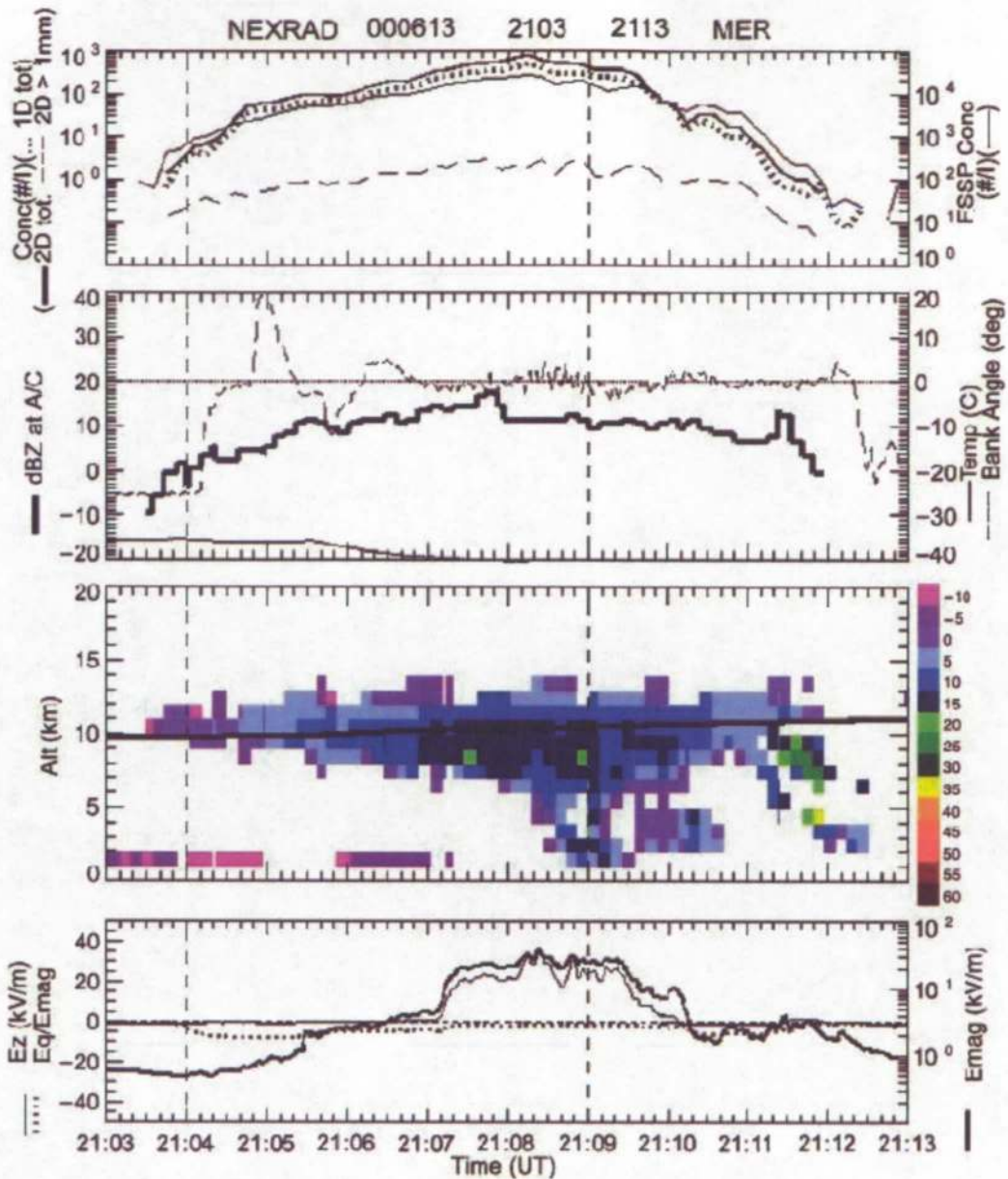
343 Comparison of the 10 and 4 km CAPPIs in Figure 1 shows that the anvil extended
344 more than 50 km to the north, northeast of the main convection. There was some weak
345 low-level convection north of the main core. The reflectivity curtain in the third panel of

346 Figure 2 near 2109 to 2110 shows precipitation falling to the ground in this region. From
 347 2103 to 2108 the penetration was in the anvil that extended to the east. It is anvils such as
 348 this that have a well defined base that are the focus of the studies described herein.



349
 350 Figure 1 CAPPIs of reflectivity at 4, 7 and 10 km MSL for the 2104 – 2109
 351 NEXRAD volume scan with the Citation track from 2102 to 2111 overlaid in red. The
 352 initial position of the aircraft is shown by a square with Xs showing each successive
 353 minute along the track. Red triangles show the positions of CG flashes detected by the
 354 CGLSS system during this volume scan. The ground projection of LDAR VHF sources
 355 are shown by black pluses.
 356

357 Figure 2 shows a MER plot (Microphysics, Electric field and Reflectivity) for the
358 10 min period including the aircraft penetration shown in Figure 1. At the Citation typical
359 flight speed of ~ 120 m/s, one minute corresponds to roughly 7 km of horizontal distance.
360 The figure shows a dramatic increase in electric field as the aircraft approached a
361 reflectivity of about 15 dBZ near 2107. The scalar magnitude of the vector electric field,
362 E_{mag} , (henceforth called the electric field magnitude) bottom panel in figure 2, increased
363 from ~ 3 kV m^{-1} to ~ 20 kV m^{-1} in about 10 s (~ 1200 m). This large, rapid increase in field
364 was a common feature of the ABFM II measurements. During this penetration the field
365 magnitude was dominated by E_z . Note that in the MER plots, E_z is plotted on a linear
366 scale shown on the left side of the figure, while the field magnitude, E_{mag} , is plotted on a
367 log scale on the right side of the figure. E_x and E_y contributed somewhat to the field
368 magnitude, but the contributions were small. The dominance of the vertical component of
369 the field was found to be true in almost all of the penetrations even when a penetration of
370 the anvil was made close to the convective core of the storm. Note that the sharp increase
371 in electric field occurs more than 3 min (~ 20 km) after the aircraft entered the anvil and a
372 minute (~ 7 km distance) before the aircraft passed over precipitation that was reaching the
373 ground (Figure 2). The measurements shown in Figure 2 are typical of those from other
374 penetrations, some of which were farther from the core and the low-level convection seen
375 on the west side of the storm in Figure 1.



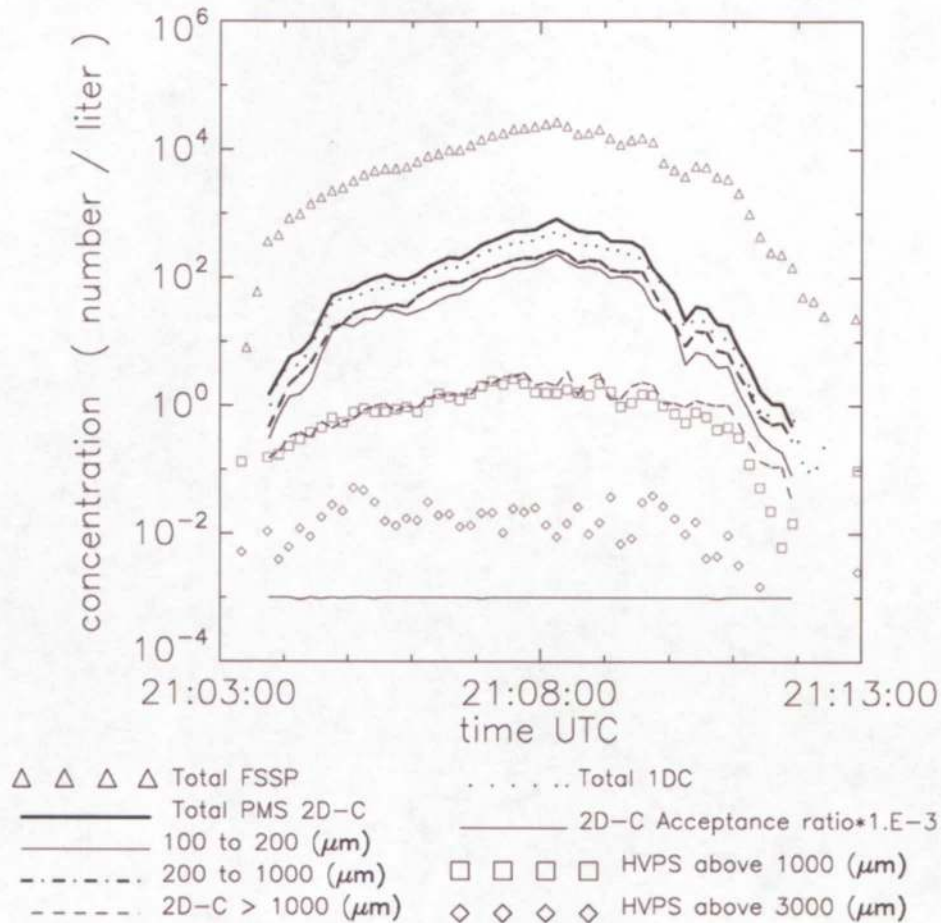
376

377 Figure 2 MER plot for 2103 to 2113 on June 13, 2000. Top Panel: Particle
 378 concentrations from different instruments: FSSP total concentration = light, solid line;
 379 2D-C total concentration = bold, solid line; 2D-C concentration >1 mm = dashed line;
 380 1D-C total concentration = dotted line. Second panel: Reflectivity at the aircraft location,
 381 bank angle of the aircraft and ambient temperature. Third Panel: Curtain of radar
 382 reflectivity above and below the aircraft (the numbers to the right of the color scale show
 383 the upper limit of reflectivity for each color interval); bold line = aircraft altitude. Bottom
 384 panel: E_z , the vertical component of electric field, is a thin line and referenced to the
 385 linear scale on the left. $E_q/Emag$, shown as a dotted line, is also referenced to the left
 386 scale. (E_q is the field due to the charge on the aircraft). $Emag$, the scalar magnitude of the
 387 vector field, is shown as a bold line and referenced to the log scale on the right.

388 Even though this pass of the Citation was moderately close to the core of the storm
389 (Figure 1) and the core was still producing lightning, the Rosemount Icing Detector
390 showed no evidence of supercooled water being present. All passes were examined for
391 evidence of the presence of any supercooled liquid water in these anvils, but none was
392 found [Schild, 2002]. We have confidence in the ability of the Rosemount probe on the
393 Citation to detect supercooled liquid water because it did show supercooled liquid water
394 to be present in some convective cores. Although supercooled water was not present at
395 the aircraft penetration altitudes of 8 to 11 km, the laboratory work of Jayaratne et al.,
396 [1983] has shown that a limited amount of charge transfer can occur between colliding
397 ice particles, albeit very, very small. Dye and Willett [2006] argue that given the broad
398 ice particle size distributions and the extended times available for particle collisions in
399 long-lived anvils some charge transfer might be occurring, but at a much slower rate than
400 occurs in convective cores.

401 Particle concentrations in different size ranges are shown in Figure 3. Unlike the
402 abrupt increase in electric field (Figure 2), the concentration of particles in different size
403 ranges did not show abrupt changes but gradually varied as the Citation flew from the
404 edge of the anvil towards the more dense part of the anvil and then decreased more
405 rapidly on the western side of the anvil. The relative increase in concentration was larger
406 for the smaller particles (shown by the FSSP and the total concentration of the 1-DC and
407 2D-C probes) than for the larger particles (shown by particles > 1 mm from the 2D-C and
408 HVPS). The concentration of particles >3mm (measured by the HVPS) changed near the
409 anvil edge, but there was not a distinct trend during most of the penetration. Note that the

410 concentrations of small and intermediate-sized particles were greatly reduced near the
 411 anvil edges as would be expected as a result of evaporation and mixing.



412

413 Figure 3 Time series plots of 10 second average values of particle number
 414 concentration for different probes and size ranges as indicated. The trace for the 2D-C >
 415 1000 μm is the dashed line almost on top of the squares for HVPS >1000 μm .

416

417 Figure 4 shows examples of images from the 2D-C for the pass of Figure 1. Images

418 of the particles from the CPI and 2D-C showed that smaller particles were primarily

419 frozen cloud droplets. The intermediate-sized particles were usually irregularly shaped,

420 but pristine crystals such as plates were occasionally seen. The particles larger than 500

421 μm were primarily aggregates or polycrystals [Bailey and Hallett, 2002]. Near convective

422 cores some rimed particles were seen. A cursory examination of CPI particle images for
 423 some of the cross-anvil penetrations did not show a change in particle type associated
 424 with the abrupt increases of electric field, but this deserves a more careful study.



425
 426

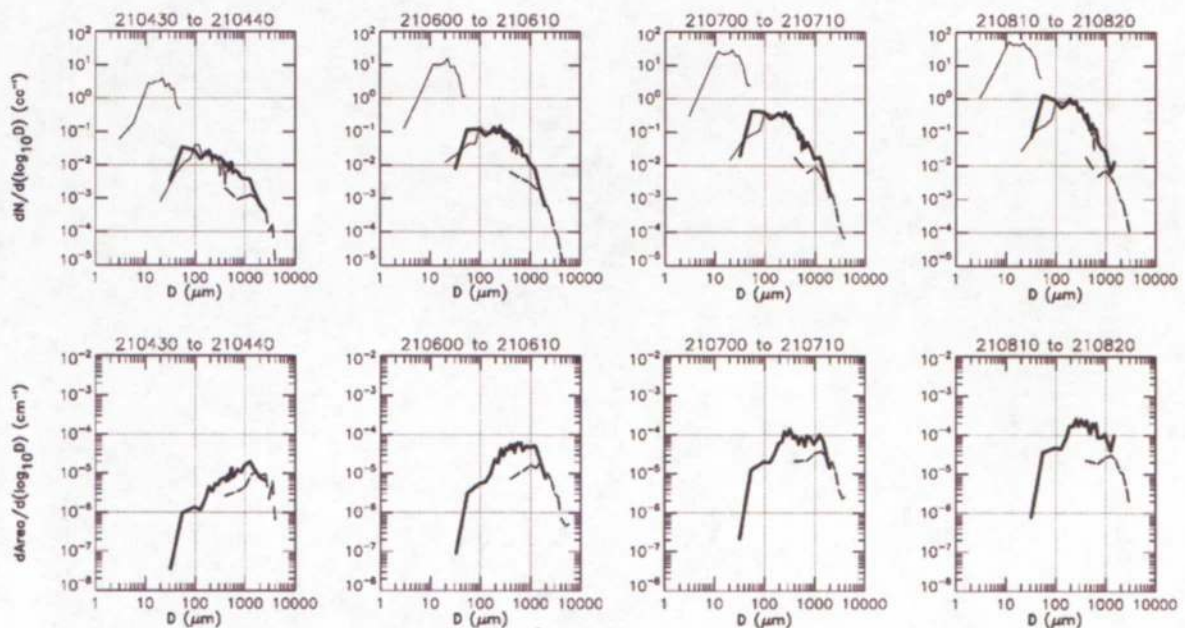
427 Figure 4 Buffers of particles imaged by the 2-DC probe. The vertical dimension of
 428 each row is ~ 1mm. Text at the top of each buffer(row) shows the flight day (M/D/Y); the
 429 start time of the first image in that buffer; the time of the last image in the buffer; DeltaT
 430 = the elapsed time to fill the buffer; TAS = true airspeed of the aircraft. Only one out of
 431 every hundred buffers recorded is displayed.

432

433 Plots of the size distributions of particle number concentration and cross-sectional
 434 area at different locations across the anvil from near the edge to the dense part are
 435 presented in Figure 5. Because both size and concentration range over a few orders of
 436 magnitude, these distributions are plotted in the form $dn_i = f_n(\log D_i) d(\log D_i)$, where dn_i
 437 is the concentration of particles in the size interval i and D_i is the mean size of particles

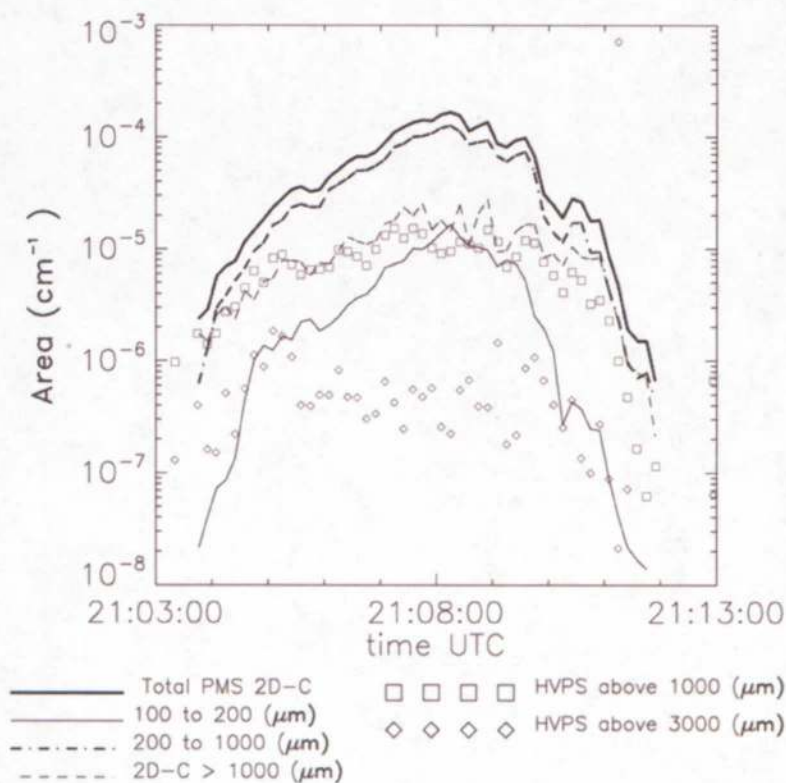
438 in that interval. dD_i/D_i was substituted for $d(\log D_i)$ because the particles are accumulated
 439 in linear size intervals. Thus, $dn_i = fn(\log D_i) dD_i / D_i$. The units of dn_i are cm^{-3} .

440 The cross-sectional area for each particle was determined from the 2D-C and HVPS
 441 images based upon the number of pixels occulted by the particle as it transited the laser
 442 beam of that probe. Particle areas were then accumulated in the same size bins as were
 443 the number concentrations. The particle size distribution plots in Figure 5 show the
 444 agreement between the different probes as well as more details of the distributions
 445 themselves. As previously noted in Figure 3, successive size distributions in Figure 5
 446 show increases over the entire size range as time progressed, reaching a peak near 2108
 447 when the Citation was flying in higher reflectivity.



448 Figure 5 Top: Particle size distributions (10 s integration times) for the periods indicated
 449 during the Citation pass shown in Figures 1 and 2. Bottom: Particle cross-sectional area
 450 distributions from the 2D-C and HVPS for the same 10 sec time periods. Light line on the
 451 left side of number plots = FSSP; bold line = 2D-C; dotted line near the 2D-C line = 1D-
 452 C; dashed line on right of each plot = HVPS.
 453
 454

455 Excluding the FSSP measurements, the mode of the number concentration plots
 456 was at sizes of 50 – 300 μm , while the mode of cross-sectional area was at sizes of 200 -
 457 2000 μm . Willett and Dye [2003] argue that the particle cross-sectional area is one of the
 458 primary factors controlling the rate of decay of electric field in the anvil. The cross-
 459 sectional particle area in different size ranges is plotted in Figure 6 for the measurements
 460 from the 2D-C and the HVPS. This figure shows that in the main body of the anvil, the
 461 area for sizes between 0.2 and 1 mm was almost one order of magnitude greater than the
 462 area for particles > 1mm in size. But near the edges of the anvil (near 2104 and 2011) the
 463 particles >1 mm contributed almost as much to the total area as the 0.2 to 1 mm particles.



464

465 Figure 6 Time series plot of 10 second average values of particle cross-sectional
 466 area in different size intervals derived from 2D-C and HVPS measurements as indicated.

467 The trace for the 2D-C >1000 μm is the dashed line almost on top of the squares for
468 HVPS >1000 μm .

469

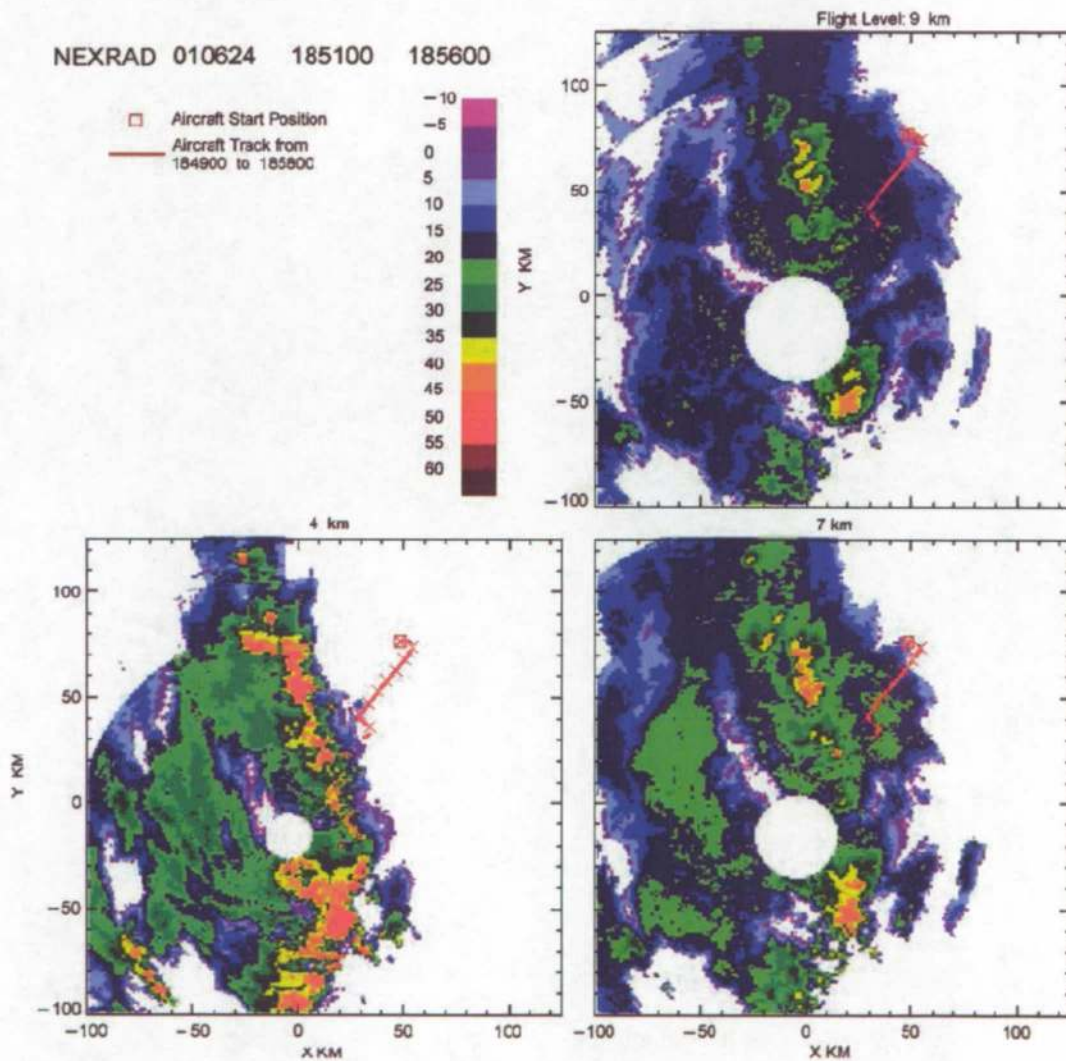
470 During this penetration across the anvil, the total particle cross-sectional area
471 increased by more than an order of magnitude from the anvil edge to the dense part of the
472 anvil. Consequently, the time expected for field decay is expected to increase by similar
473 amounts. Calculations for this penetration presented by Willett and Dye [2003] of “E
474 Time Scale”, an estimated upper bound on the time required for the electric field
475 magnitude to decrease from 50 to near 0 kV m^{-1} based on an observed particle size
476 distribution, gave E Time Scale values of ~ 300 s (5 min) at the anvil edge but ~ 5700 s
477 (93min) in the dense part of the anvil near 2108. Thus, at the edge of anvils the electric
478 field decay should be very rapid but the decay is expected to be much, much slower in the
479 dense part of the anvil. Because sedimentation and turbulent mixing, leading to
480 evaporation, are the main mechanisms acting to erode the particle size distribution, the
481 rates of mixing and sedimentation may also be important factors in determining the
482 electric field decay.

483

484 3.2 24 June 2001

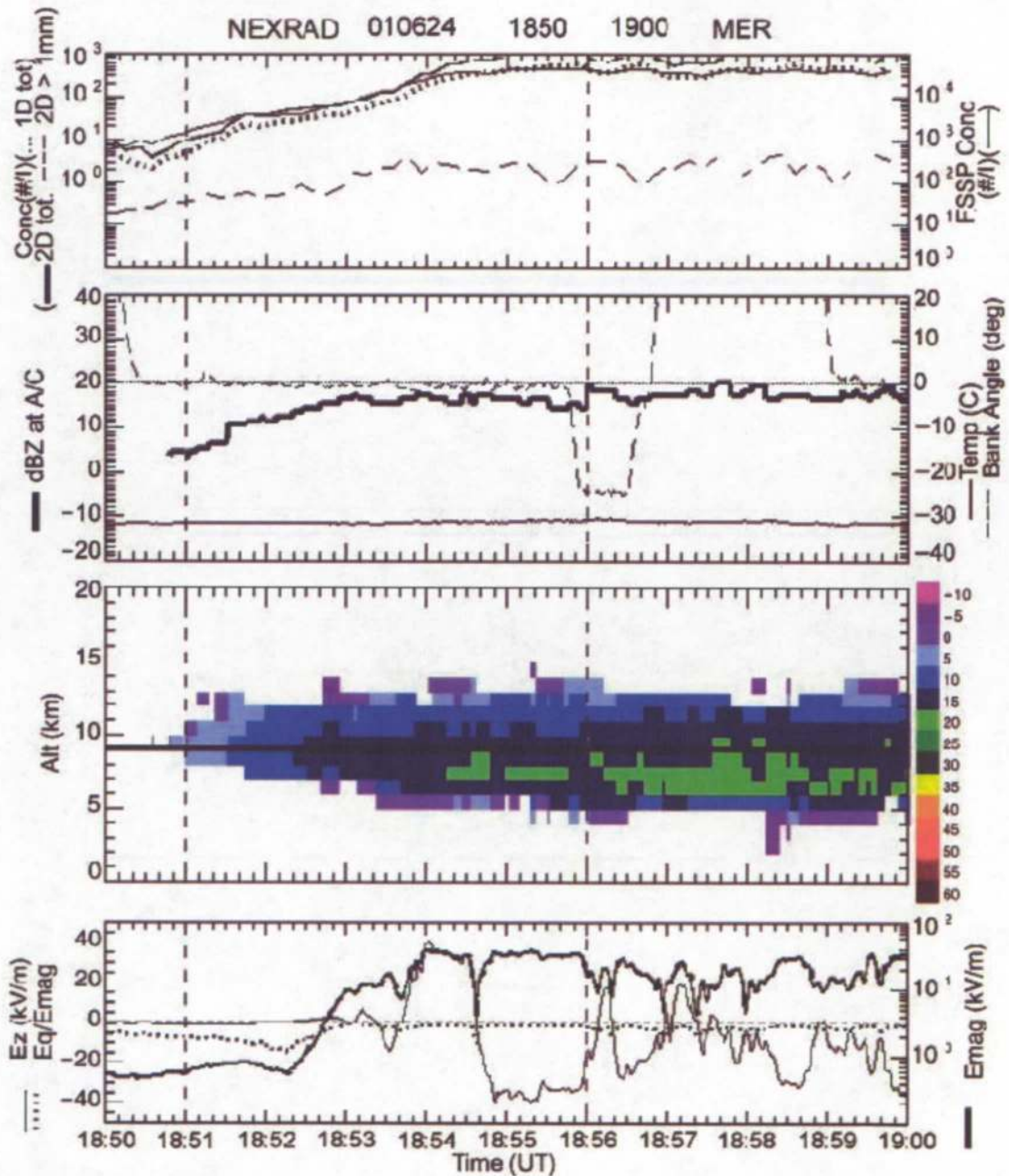
485 On June 24th wide spread convection started at 1630 with a cold front approaching
486 from the north. By 1800 storms covered central Florida with a line of strong convection
487 oriented along the east coast moving over KSC and Cape Canaveral. One of these cells
488 spawned a tornado that touched down in the Eastern Range at 1830. The Citation took off
489 at 1803 and almost immediately climbed into an anvil that extended 40 km to the
490 northeast of KSC. It then made several penetrations in the northeast and southwest

491 directions moving away from and towards the line of convective cores, along and into the
492 direction of the wind. The track of the aircraft toward the convection from 1849 to 1858
493 is shown overlaid on CAPPi in Figure 7. The figure shows the anvil ahead of the line of
494 convection and a trailing stratiform region behind the line, characteristics of mesoscale
495 convective systems. The corresponding MER plot of particle concentration, reflectivity
496 curtain along the aircraft track and electric field measurements is presented in Figure 8.



497
498

499 Figure 7. CAPPis of reflectivity at 4, 7 and 9 km for June 24, 2001 from the
 500 NEXRAD 1851 to 1856 volume scan with aircraft track from 1849 to 1858 overlaid in
 501 red. The initial aircraft position is shown by a square with Xs plotted at each successive
 502 minute along the track.



503
 504

Figure 8 Same as figure 2 except 1850 to 1900 on June 24, 2001.

505

506 Figure 8 shows an example of the changes in electric field observed when
507 penetrations were made from the downwind tip of the anvil towards the convective core
508 along the anvil axis. Particle concentrations and reflectivity increased smoothly from the
509 edge of the anvil inward but there was an abrupt, rapid increase in electric field (between
510 1852 and 1853) even in this intense storm, which was very actively producing lightning
511 at the time of this penetration. As with the June 13th case of Figure 2, the field increase
512 occurred near a reflectivity of 10 to 15 dBZ. The bottom panel of Figure 8 shows large
513 variability and changes in polarity of E_z during this constant altitude pass, indicating the
514 complex charge structure of this anvil.

515 Some of these field changes were probably produced by nearby lightning. The
516 LDAR VHF sources (not shown) showed that lightning extended out almost as far as the
517 western end of the Citation track at ~1858. The particle concentrations measured by the
518 2D-C on June 24th (Figure 8) are a little higher than the maximum total 2D-C
519 concentration shown in Figure 2 for June 13th, but considering the intensity of this storm
520 were rather comparable. The electric field magnitude was also comparable for the two
521 cases.

522

523 4. Synthesis of Measurements in Anvils

524 In the previous section we showed examples of the electric field, particle
525 concentration, and radar reflectivity measurements for two separate anvils. In this and
526 following sections we examine the relationships between these parameters for all of the
527 ABFM II measurements in anvils. To examine these relationships we produced a dataset

528 for each Citation flight that included 10 s averages of measurements of standard state
529 parameters; such as ambient temperature, aircraft altitude, attitude and position; the three
530 components and magnitude of the electric field; and particle concentrations in different
531 size categories for each of the particle probes. These airborne measurements were then
532 merged with measurements of the reflectivity at the aircraft location and other spatial
533 averages of reflectivity centered on the time and position of the aircraft. In this section, in
534 order to reduce the statistical uncertainty in the particle concentration measurements and
535 the point-to-point scatter in reflectivity values, we have used 30 s averages of aircraft
536 measurements and 3-km cube averages of reflectivity. At a flight speed of 100 to 120 m
537 s^{-1} 30 s corresponds to a distance of 3.0 to 3.6 km.

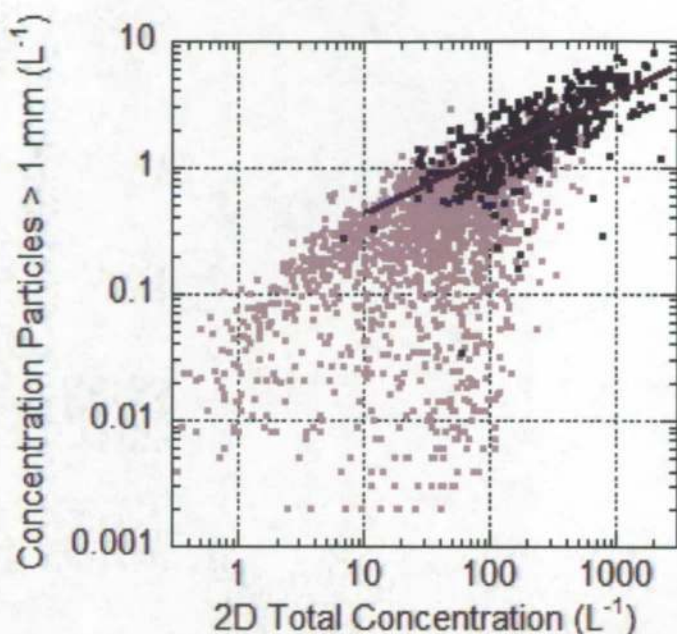
538 Although several different types of clouds were sampled by the aircraft during the
539 ABFM II project, we present here only those measurements made in or near anvils. We
540 defined an anvil as a cloud formed by transport away of material from the convective
541 core(s) by upper level winds or divergence at the top of a convective core. To be
542 considered an anvil, we further required that the cloud in question had a radar definable
543 base without precipitation reaching the ground. This then excluded some measurements
544 that were made during penetrations near convective cores where precipitation was
545 reaching the ground or in precipitating stratiform regions. The total number of 30 s
546 averages in this composite data set of anvil measurements was 2190 from 29 different
547 anvils and 79 separate penetrations. Most of the aircraft penetrations were at altitudes of
548 8 to 10 km.

549

550 4.1. Similarity of the Microphysical Properties of Dense Anvils

551 The microphysical measurements in the dense part of the anvils, i.e. the regions
552 with the highest reflectivity and greatest particle concentrations showed a lot of similarity
553 from flight to flight and anvil to anvil. This is in part because >65% of the measurements
554 in anvils made during ABFM II were at altitudes of 8 to 9.3 km. The similarity in the
555 particle size distributions in the dense part of the anvils is shown in Figure 9 where the
556 concentration of particles > 1 mm measured by the 2D-C for each 30 sec period is plotted
557 versus the total concentration of particles measured by the 2D-C. The measurements were
558 broken into 2 groups, those with field magnitudes $\geq 10 \text{ kV m}^{-1}$ (black) and those with
559 field magnitudes $< 10 \text{ kV m}^{-1}$ (gray).

560 Figure 9 shows that there is an almost linear relationship in this log-log plot in the
561 dense part of the anvils where the field magnitude was $> 10 \text{ kV m}^{-1}$. A linear least square
562 fit to the logarithms of those points with field magnitude $\geq 10 \text{ kV m}^{-1}$ (the 456 black
563 points) had a correlation coefficient of 0.69, which has high statistical significance. This
564 best fit line shows almost two orders of magnitude increase of the total 2D-C
565 concentration for each order of magnitude increase in the concentration of particles
566 greater than 1 mm. This result is similar to that shown in Figure 3 for only one
567 penetration, i.e. as the aircraft flew from the edge of the anvil toward the dense part of the
568 anvil the concentration of small and intermediate-sized particles increased more than the
569 concentration of the larger particles.



570

571

572

573 Figure 9 Scatter-plot of 30 sec averages of total particle concentration measured
 574 by the 2D-C vs. the concentration of particles > 1 mm measured by the 2D-C. The points
 575 with field magnitude $\geq 10 \text{ kV m}^{-1}$ are plotted in black while those with field $< 10 \text{ kV m}^{-1}$
 576 are gray. There are a total 1998 points in this plot of which 456 points had field
 577 magnitudes $\geq 10 \text{ kV m}^{-1}$. The straight line is a least square fit to only those points with
 578 $E \geq 10 \text{ kV m}^{-1}$.

578

579

580 Although there is scatter, the variation of particle concentration from case to case
 581 was within a factor of 2 to 3 in the dense anvils. In the edges of the anvil where
 582 concentrations are smaller, there was much more variation. The majority of the points
 583 with high concentrations of both small and large particles were the same regions with
 584 fields magnitude $> 10 \text{ kV m}^{-1}$. Contrastingly those regions with lower particle
 585 concentrations corresponding to edges or other less dense parts of the anvil were almost
 586 devoid of points with field $> 10 \text{ kV m}^{-1}$.

586

587 Both aggregation and sedimentation should alter the particle size distribution in an
 588 anvil and we have some evidence of this in the measurements made during spiral
 descents. On 24 June 2001 a descent was made from 9.2 to 4.7 km (-31 to -4 °C) from

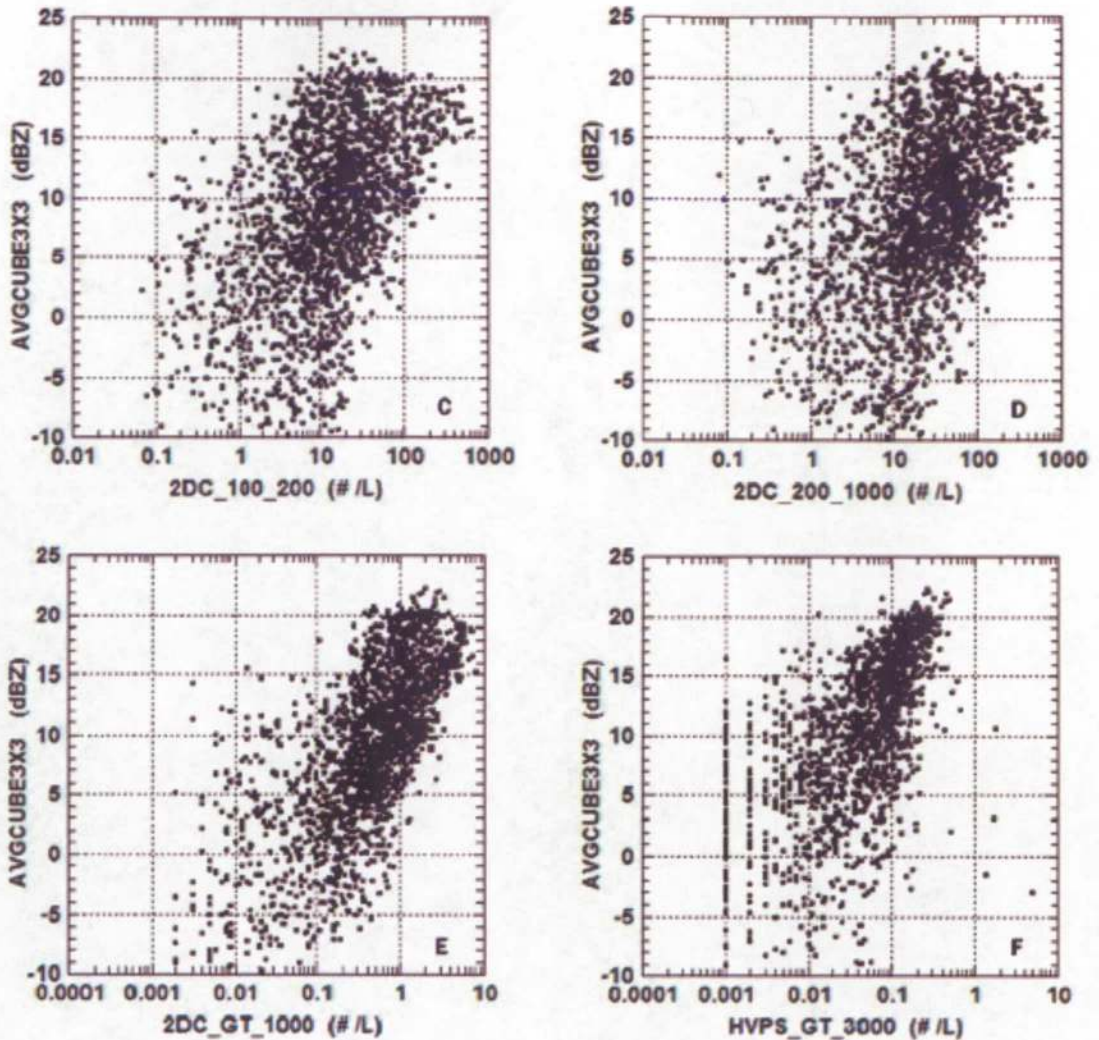
589 1947 to 2001 in a region that was the transition zone between the anvil and a broad mid-
590 level stratiform region with 20 - 25 dBZ reflectivity at 6 - 8 km altitude, but without
591 precipitation reaching the ground. The electric field magnitude was $10 - 30 \text{ kV m}^{-1}$ for
592 much of the descent. The concentration of the small and intermediate-sized particles
593 decreased by a factor of 3 to 4 and the concentration of the particles $>3 \text{ mm}$ increased by
594 a factor of about 5, thus showing the effects of sedimentation and aggregation. The
595 concentration of particles $>1 \text{ mm}$ increased less than a factor of 2. In the altitude interval
596 of 9.2 to 8 km, where $>65\%$ of the ABFM II anvil penetrations were made, the decrease
597 in small to mid-sized particles was small and the increase in $>3\text{mm}$ particles was less
598 than a factor of 2.

599

600 4.2 Relationship between Radar Reflectivity and Particle Concentration

601 Figure 10 shows the average reflectivity in a 3-km cube centered on the aircraft
602 altitude and location plotted as a function of particle concentration for different size
603 ranges. The reflectivity of the 1-km grid pixels was averaged in dBZ and pixels with no
604 detectable reflectivity or reflectivity $<0 \text{ dBZ}$ were not included in the average. To be
605 included in the data set, we required that at least 16 of the 27 one kilometer pixels in the
606 3-km cube contain reflectivity above a threshold of 0 dBZ. Three kilometers was chosen
607 as it approximately corresponded to the distance flown by the aircraft in 30 s. In addition,
608 the 3-km cube average smoothed some of the pixel to pixel variation of the 1-km gridded
609 radar measurements and also helped to compensate for the scan gaps in radar coverage
610 when the radar elevation sweeps did not overlap.

611



612
 613
 614
 615
 616
 617
 618
 619
 620

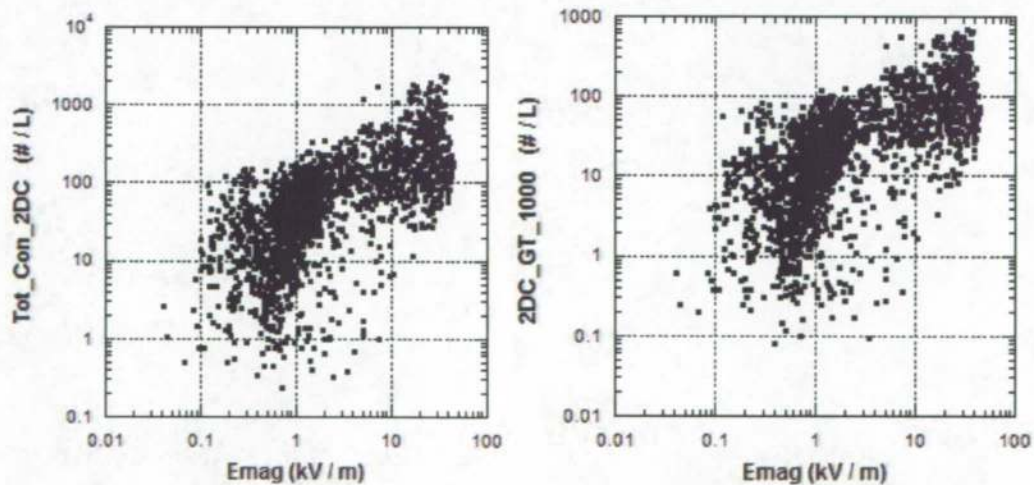
Figure 10 Scatter-plots of particle concentrations in different size categories (100-200 μ m; 200-1000 μ m; 2D-C \geq 1mm; and HVPS \geq 3mm) vs. the average reflectivity within a 3-km cube centered on the altitude and position of the aircraft. There were about 2000 points in C, D, and E and 1500 in F.

621 Although there is a lot of scatter in these plots, particularly for the 100-200 μ m and
 622 200-1000 μ m particle size ranges, all plots showed a trend of increases in reflectivity
 623 with increases in concentration in all size ranges. Linear least square fits to the
 624 reflectivity in dBZ vs. the logarithm of particle concentration gave correlation
 coefficients of 0.50, 0.58, 0.68 and 0.58 for plots C, D, E and F, respectively. Although

625 the correlation coefficient of plot F (for the concentration of particles >3 mm) is less than
626 that for plot E (for the concentration of particles >1 mm), visually there appears to be less
627 scatter in plot F for points with the greatest particle concentration. Because the radar
628 reflectivity is proportional to the sixth power of particle size, we expect the reflectivity to
629 be dominated by the concentration of the largest particles, as suggested in Figure 10. The
630 ABFM II observations in these Florida anvils do not show unusual behavior in the
631 relationship between particle concentration and reflectivity. Figure 10 is shown here
632 primarily to help interpret the results of the next two sections, where the electric field
633 magnitude is shown not to have a well behaved relationship to either particle
634 concentration or radar reflectivity.

635 4.3 Relationship between Electric Field and Particle Concentration

636 The relationship between electric field and particle concentration is shown in Figure
637 11. Unlike the trend of increasing reflectivity with increasing particle concentration
638 shown in Figure 10, both the total 2D-C concentration and the concentration of particles
639 > 1mm shown in Figure 11 exhibit a clear change in character at 1 to 2 kV m^{-1} . For



640
641 Figure 11 Scatter-plot of electric field vs total particle concentration measured by
642 the 2D-C (left) and concentration of particles > 1 mm size (right) for the ABFM II anvil

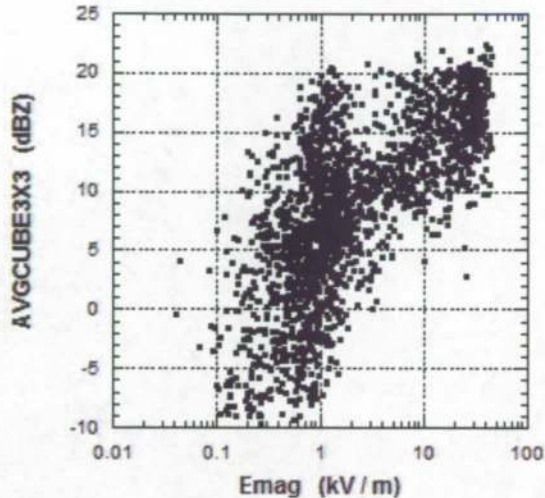
643 data set. Each figure contains about 2100 separate 30 sec averages. Note that the
644 concentration scale is different in the two plots.
645
646 electric fields $> 2 \text{ kV m}^{-1}$ there was a gradual, but not pronounced, increase in the particle
647 concentrations as electric field increased from 2 to $>30 \text{ kV m}^{-1}$. But for electric fields < 2
648 kV m^{-1} there is a “knee” and much more variation in the particle concentration. This knee
649 is a result of the rather abrupt transition in electric field noted previously and shown in
650 Figures 2 and 8. The plots show a threshold behavior with only a few points in the lower
651 right part of the plots. The points in Figure 11 are distributed throughout the anvil cases.
652 Thus the knee in these plots was not from any specific case but was a feature that is
653 representative of all the ABFM II anvil measurements. This change in behavior suggests
654 a change in physical processes or perhaps in the balance between different physical
655 processes. We will explore some possible explanations for this change in behavior in
656 Section 6 below.

657

658 4.4 Relationship between Electric Field and Reflectivity

659 The relationship between the electric field magnitude and the 3-km cube average
660 reflectivity is presented in Figure 12. Like the plots of particle concentration versus field
661 magnitude shown in Figure 11, these plots show a change of character or knee at 1 to 2
662 kV m^{-1} . This is not too surprising in view of the monotonic trends shown in Figure 10
663 above. For electric fields less than 2 kV m^{-1} , the average reflectivity spanned a range
664 from -10 to $>20 \text{ dBZ}$ with many points having a field $< 3 \text{ kV m}^{-1}$ but a reflectivity of 10
665 to 20 dBZ, showing that higher reflectivity is not necessarily a good predictor of strong
666 electric fields. However, only a few points with electric field $>3 \text{ kV m}^{-1}$ have a

667 reflectivity less than 5 dBZ. There is a reflectivity threshold below which thunderstorm
668 strength electric fields ($>\sim 5 \text{ kV m}^{-1}$) were not found in ABFM II anvils.
669



670
671 Figure 12 Scatter-plot of electric field magnitude vs. 3x3x3 km cube average
672 reflectivity for the ABFM II anvil data set.
673
674

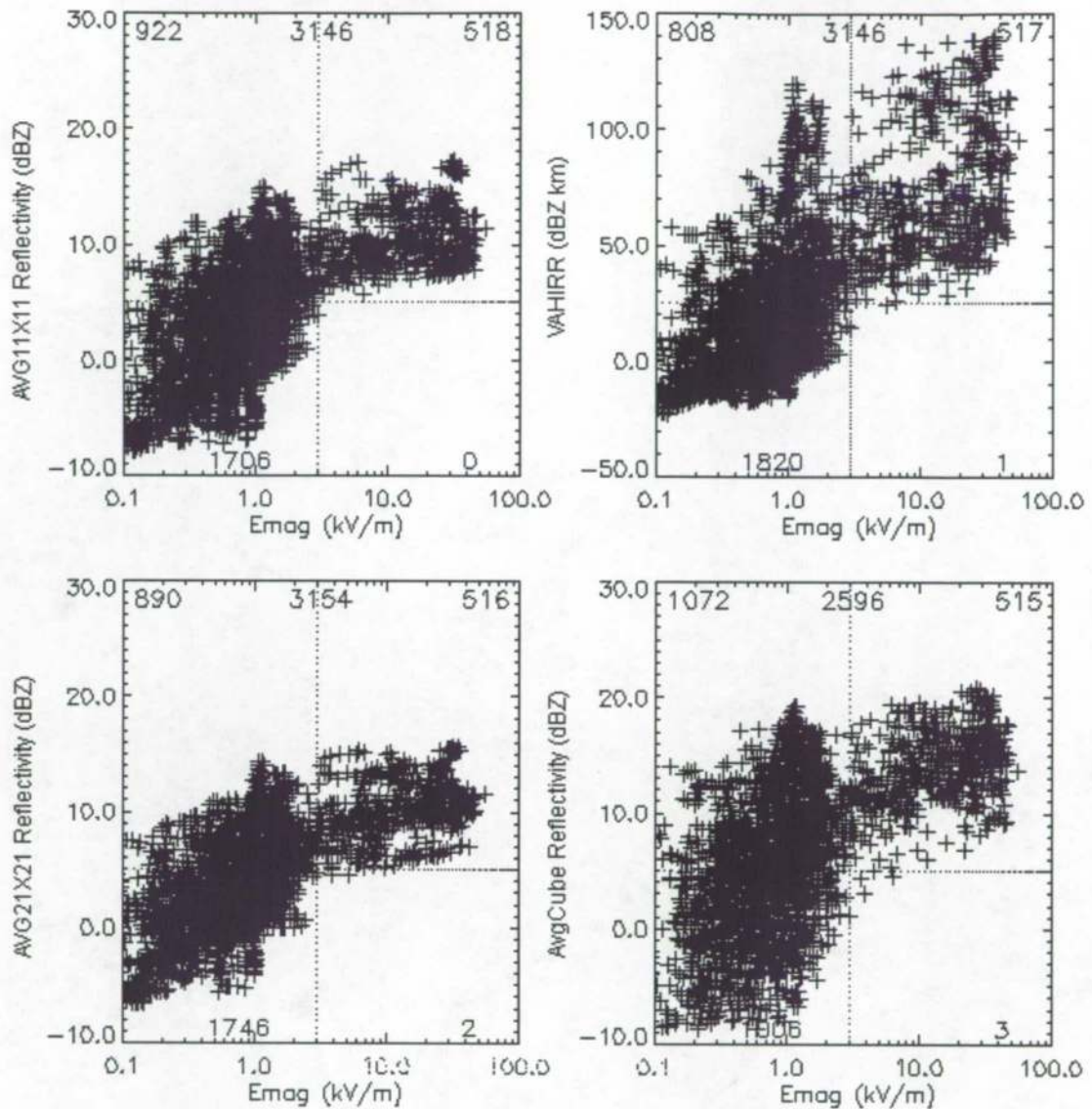
675 5. Exploring Possible Radar Parameters for Use in an LLCC

676 The results shown in Figure 12 gave promise that a radar-based reflectivity
677 parameter might be a useful diagnostic for determining the possibility of high electric
678 fields in anvils and for developing improved Lightning Launch Commit Criteria (LLCC)
679 for anvils. However, since there were a few points in the lower right quadrant of Figure
680 12 that had electric fields $>3 \text{ kV m}^{-1}$ with average reflectivity less than 5 dBZ, we
681 explored other possible spatial averages of reflectivity.

682 Before examining other radar parameters we wanted to know the maximum electric
683 field that might present a threat for triggering lightning in these anvils. This is a topic of
684 current research and a detailed discussion is beyond the scope of this paper. Extrapolation
685 of the rocket triggered lightning studies of Willett et al. [1999] to anvil altitudes

686 suggested that electric fields $<3 \text{ kV m}^{-1}$ are not capable of triggering lightning to large
687 vehicles like the Space Shuttle and the Titan booster at anvil altitudes. This is the value
688 currently used by the Air Force and NASA in the existing LLCC. By way of comparison,
689 during ABFM II in dense parts of anvils field magnitudes of $30 - 60 \text{ kV m}^{-1}$ were
690 frequently observed during penetrations near the convective cores of storms and $10 - 30$
691 kV m^{-1} in anvils tens of kilometers downwind of the core. Fields of $100 - 150 \text{ kV m}^{-1}$
692 have often been observed in mature thunderstorms [MacGorman and Rust, pp. 174 – 177,
693 1998].

694 Figure 13 shows the relationships between electric field and 4 different spatial
695 averages of reflectivity. In these plots we have used 10 s averages of electric field and we
696 have filtered the entire anvil data set to remove points for which the aircraft was within
697 20 km of a convective core with reflectivity $>35 \text{ dBZ}$ at 4 km altitude or greater in order
698 to avoid regions of rapid field intensification associated with the cores. We also have
699 removed points for which the aircraft was within 20 km of any lightning detected by
700 either LDAR or the CGLSS within the previous 5 min in order to avoid regions directly
701 influenced by recent lightning. Additionally, we limited these averages of reflectivity to
702 altitudes $\geq 5 \text{ km}$, roughly the freezing level in Florida during the summer. The plot on
703 the lower right shows results for the 3-km cube reflectivity average and is similar to
704 Figure 12 except for the core and lightning filters mentioned above and except for 10 s
705 averages of electric field rather than the 30 s averages used previously. The results are
706 similar to those of Figure 12 with a few points that have $E >3 \text{ kV m}^{-1}$ and reflectivity <5
707 dBZ .



708

709

710

711

Figure 13 Electric field magnitude (E_{mag}) versus reflectivity for 4 different spatial averages of reflectivity. (See the text.) The number in the top center of each plot gives the total points in that plot with the numbers near the corners of each plot showing the number of data points in each quadrant of that plot. The text at the top indicates which data set and what filtering was used.

712

713

714

715

716

717

A reflectivity parameter averaged over a volume larger than 1-km or 3-km cube

718

has the possibility of including regions of high reflectivity that might contain substantial

719 charge near, but not at the aircraft position. It has the additional advantage that averaging
720 over a larger volume will compensate for any unsampled scan gaps and radar propagation
721 effects. The upper left plot labeled AVG 11x11 Reflectivity on the ordinate shows the
722 average dBZ reflectivity calculated from 5 km altitude (approximately the 0C level) to
723 the top of the cloud over an 11 x11 km area extending horizontally 5 km in the north,
724 south, east and west directions from the 1 km grid point containing the aircraft position.
725 The lower left plot labeled AVG 21x21 Reflectivity on the ordinate is similar except that
726 the volume average is calculated over an area extending 10 km in each direction from the
727 aircraft position. These 2 plots show very similar results.

728 A shortcoming of the volume averages is that averaging the reflectivity within a box
729 or column ignores potentially important information on the depth of the anvil. A thin
730 anvil might have the same average reflectivity as a much deeper anvil, but deeper anvils
731 are more likely to contain charge. The upper right plot of Fig. 13 shows the 11x11
732 Volume Averaged Height Integrated Radar Reflectivity (VAHIRR) [Bateman et al.,
733 2005]. This parameter was calculated by multiplying the 11x11 reflectivity averaged in
734 dBZ by the average radar thickness of the anvil in km over the 11x11 km area. Unlike the
735 11x11 average reflectivity plot, in the upper right quadrant the 11x11 VAHIRR plot
736 shows high values of reflectivity with high values of field magnitude. It has only one
737 point in the lower right quadrant for VAHIRR <25 dBZ km and electric field >3 kV m⁻¹.
738 A statistical analysis of extreme values [Reiss and Thomas, 2001] by Dr. Harry C. Koons
739 (Personal communication) for the 11x11 km VAHIRR ≤ 10 dBZ km (equivalent to an
740 average of 10 dBZ in a 1 km thick anvil, or 2 dBZ in a 5 km thick anvil) showed that the
741 probability of having an electric field >3 kV m⁻¹ was less than 1 in 10,000. VAHIRR is

742 now being used by the Air Force and NASA in new Lightning Launch Commit Criteria
743 for anvils.

744

745 6. DISCUSSION

746 In previous sections we have shown that along a penetration the electric field
747 increased abruptly in contrast to the more smoothly changing particle concentrations or
748 reflectivity. This behavior was apparent for individual penetrations as well as in a
749 statistical sense for all of the anvil measurements. In this section we explore possible
750 causes for this behavior.

751

752 6.1 Screening Layers

753 At cloud boundaries the electrical conductivity changes significantly. If there is a
754 component of electric field normal to the cloud boundary fast ions can attach to cloud
755 particles to produce charge layers that tend to "screen" the outside air from elevated fields
756 in the lower-conductivity interior of the cloud [e.g., Klett, 1972], hence the name
757 screening layer. Vonnegut *et al.* [1966] and Blakeslee *et al.*, [1989] have measured strong
758 electric fields above the top of convective regions of thunderstorms and have concluded
759 that screening layers were not present in the convective turrets because of rapid mixing
760 and entrainment near the cloud boundaries. At the top and bottom of stratified anvil
761 clouds that contain net charge, however, balloon-borne measurements have found
762 screening layers a few hundred meters thick [e.g., Winn *et al.*, 1978; Marshall *et al.*,
763 1984; Byrne *et al.*, 1989]. In principal, such layers might build up around the entire

764 periphery of an electrified anvil, *i.e.*, on the vertical edges as well as on the top and
765 bottom.

766 There are two cases that concern us here. First, our observations of abrupt increases
767 in field magnitude when flying horizontally into anvils might be due to vertical screening
768 layers on the edges of these clouds. Such a vertically oriented charge layer near a cloud
769 boundary could only be caused by a significant horizontal component of the field from
770 net charge in the interior. If it existed, this layer of charge would produce a change in the
771 horizontal field component perpendicular to the cloud edge as the aircraft penetrated the
772 cloud.

773 There are several reasons to doubt this explanation of our observations. We are not
774 aware of any other measurements in the literature that document screening layers on the
775 vertical edges of anvils. Our ABFM II measurements of the three components of electric
776 field clearly show that the vertical component of the field, E_z , is almost always dominant
777 and usually a factor of 3 to 10 times or more as great as the E_x or E_y component. Because
778 the Citation penetrations were approximately perpendicular to the edge of the anvil, we
779 should be able to detect the presence of a vertical screening layer as an abrupt increase in
780 the magnitude of E_x on entering or exiting the anvil, but we do not. Furthermore, the
781 abrupt change in field magnitude was often observed at large distances from the edge of
782 the anvil. For example, at 2107 in Figure 2 the abrupt field increase (primarily due to the
783 vertical component) occurred more than three minutes (~ 22 km) after the aircraft entered
784 the anvil. It is hard to imagine that turbulent mixing from the cloud edge would transport
785 screening-layer charge this far from the edge of the anvil and still maintain the sharp
786 gradient in field. Similarly, for July 24th the abrupt increase was $>2\frac{1}{2}$ min (~ 16 km) from

787 the downwind anvil tip detected by the particle probes. Merceret et al. [2006] show that
788 for ABFM II anvils the average distance inside the anvil boundary at which the field
789 magnitude exceeded 3 kV m^{-1} was about 3 km.

790 The second case that concerns us here involves the horizontal screening layers that
791 are known to occur on the top and bottom boundaries of electrified anvils. During a
792 horizontal pass through such an anvil, the aircraft might dip into or out of a charge layer
793 that was not perfectly flat as a result of gravity waves or other dynamics within the cloud.
794 If the screening layer was sufficiently thin, this might result in the kind of abrupt
795 increases and decreases in field magnitude (dominated by the vertical component of the
796 field) that we observed, for example, in Figure 2.

797 We also doubt this as an explanation of the abrupt field increases that we observed.
798 In most cases when these events occurred, the Citation was flying well below (above) the
799 top (bottom) of the anvil. For example, in Figure 2 at 2107 the abrupt field change
800 occurred where the anvil thickness was 6 to 7 km and the aircraft was at least 2 km below
801 the cloud top. Again, it is hard to imagine that turbulent mixing would transport screening
802 layer charge this far from the top of the anvil and still maintain the sharp gradient.
803 Turbulent mixing would act to smear out charge and smooth out the gradient of electric
804 field. Similarly, for July 24th the abrupt increase was approximately in the vertical center
805 of a 7 km thick anvil. In summary, it does not seem possible that screening layers could
806 explain an appreciable fraction of the sudden increases (and decreases) in field magnitude
807 that were observed during ABFM II.

808

809 6.2 Charge Transport from the Storm Core

810 Charge separation via the non-inductive mechanism is thought to occur primarily in
811 moderate updrafts or updraft/downdraft transition zones because that is the region in
812 which supercooled liquid water, graupel and numerous smaller ice particles coexist [e.g.
813 Dye et al. 1986]. Since moderate updrafts and updraft/downdraft transition zones occupy
814 only a fraction of the horizontal area of the core of a storm, it seems reasonable to expect
815 that strong electric fields would not be present across the entire breadth of the anvil, even
816 near the convective core. The ABFM II measurements made near or only slightly
817 downwind of a storm core (such as seen in Figure 2 for the June 13th case) indeed showed
818 that strong fields did not exist across the entire anvil.

819 If the abrupt changes in electric field occurred only during the cross anvil
820 penetrations, the limited extent of charge transport could explain the behavior of our
821 electric field versus particle concentration plots. However, Figure 8 for July 24, 2001
822 clearly showed an abrupt increase in electric field even when the aircraft flew along the
823 main axis of the anvil toward the core of the storm. The updraft cells in multi-cellular
824 storms, such as those investigated in ABFM II, often have lifetimes of 15 to 30 min and
825 are episodic in nature, with new updrafts forming and intensifying while others are
826 decaying. Evidence of this was clearly seen in the evolution of the reflectivity structure of
827 ABFM II storms. Consequently, the time periods of charge separation and outflow of
828 charged particles into the anvil should also be episodic. One would therefore expect that
829 the charge distribution in the anvil would be granular with some regions containing more
830 charge (stronger electric fields) than others. We see evidence of this in ABFM II
831 measurements. As a parcel containing charge moves downwind in the anvil, turbulent
832 mixing and electric field decay (see below) occur. These processes should reduce the

833 gradient of electric field as well as the magnitude and thus the abruptness of electric field
834 changes. Both the limited fraction of the storm core from which charged particles are
835 advected, and the episodic nature of the updrafts are likely to play a role in explaining
836 some of the abrupt changes in field that we observe.

837

838 6.3 The Rate of Decay of Electric Field by Conduction

839 In a passive anvil, i.e. an anvil in which active charge separation is not occurring,
840 the electric field should decay as the charge moves downwind of the convective core.
841 Willett and Dye [2003] describe a simple model to estimate an upper limit to the decay
842 time of electric field in a passive anvil in which there is a constant influx of cosmic rays,
843 no turbulent mixing, no condensation, no evaporation or sedimentation of particles and
844 the absence of active charge separation. The mechanism for field decay in the model is
845 the bulk conduction current inside the anvil that reduces the net charge contained in its
846 interior. A modification of this simple model was used to estimate an upper limit to the
847 decay time of electric field which would be expected for the along-axis anvil penetration
848 shown in Figure 8. This case is particularly amenable to model analysis because the
849 aircraft penetration from 1850 to 1856 was oriented upwind, from the tip of the anvil
850 toward the convective core. Assuming that the anvil structure remained approximately
851 steady state (which radar observations show to be valid), both electric field and particle
852 concentration would decay while moving from the core to the anvil edge, but remain
853 essentially constant at each location along the aircraft track. In the calculations The
854 actually observed particle size distributions were used for the calculation.

855 The results from the model gave a decay of electric field from 37.5 to 12 kV m⁻¹
856 over a distance of 28 km compared to an observed decay from 37.5 to <1 kV m⁻¹ in ~10
857 km. Additionally the decay in the model was continuous and not nearly as rapid as the
858 observed decay and sharp decrease in field seen between 1852 and 1853 in Figure 8. We
859 conclude that decay of electric field due to conduction currents is inadequate alone to
860 account for the abrupt changes in electric field that we observed in this or other cases.

861

862 6.4 Enhancement of Electric Field in Long-Lived Anvils

863 In a separate paper Dye and Willett [2006] show that two of the long-lived ABFM
864 II anvils developed horizontally extensive regions in which the electric field, the
865 reflectivity and the particle concentrations became very uniform and maintained strength
866 over tens of minutes and tens of kilometers. They argued that charge separation occurring
867 in the melting layer might be partially responsible for the prolongation of electric field in
868 the long-lived anvils. However, because of the long time for ice particle interactions and
869 the broad particle spectrum, charge separation might also have taken place at higher
870 altitudes than the melting zone from either a non-inductive or perhaps even an inductive
871 charge separation mechanism involving ice particle collisions. Although the non-
872 inductive mechanism has been found to be most efficient when supercooled water is
873 present, the work of Jayarante et al. [1983] and others does show some charge separation
874 can occur, albeit very much smaller, even without the presence of supercooled liquid
875 water.

876 Dye and Willett [2006] also inferred that a weak updraft must have been present in
877 the two long-lived anvils. Unfortunately the wind measurements from the Citation were

878 not reliable and often unusable, primarily because of the mass of ice particles ingested
879 into the pitot tubes.

880 The strong fields observed in the enhanced portion of the anvils seemed to be
881 associated with horizontally extensive (many 10s of km) regions of 20 to 25 dBZ at 7 km.
882 If the enhancement occurred in specific locations and not across the entire anvil, it is
883 possible that the weak fields outside the enhanced regions would reflect the values
884 expected from field decay in a passive anvil. However, when the aircraft entered the
885 enhanced parts of the anvils there might be an abrupt increase in field along the track.
886 Localized enhancement could perhaps explain the abrupt increases in field for the aircraft
887 penetrations in enhanced anvils such as 13 June 2000 and 4 June 2001. On the other
888 hand, because the particle size distributions were observed to change slowly and
889 smoothly one would think that spatial changes in the resulting ice particle collision rates
890 would also occur slowly and not lead to abrupt spatial changes in the charge structure and
891 hence electric field.

892

893 7. CONCLUDING REMARKS

894 This paper describes the ABFM II project which investigated electric fields,
895 microphysics and reflectivity in anvils, debris clouds, and regions with stratiform
896 precipitation. It has focused on the anvil measurements and presents examples for two
897 cases to illustrate the type of measurements made during ABFM II. The observations
898 have shown that electric fields in anvils often increased from weak to strong much more
899 abruptly than particle concentrations and reflectivity.

900 In Section 6 we explored several reasons for the abrupt behavior of the electric field
901 in relationship to particle concentration, and hence reflectivity. We suggested that the
902 abrupt behavior in field observed for most of the cross anvil penetrations in passive anvils
903 might be the result of the limited area of the storm core from which charged particles
904 were being advected into the anvil. Additionally, the episodic nature of the updraft and
905 hence charge advection from the core may explain some of the along-axis anvil
906 observations. In long-lived anvils in which charge separation and subsequent
907 development had occurred, the abrupt increases in electric field might be due to localized
908 regions of charge separation, but this seems at odds with the smoothly varying particle
909 concentration. The rapid rate of decay of electric field near the anvil edge due to
910 conduction currents probably also made a contribution, but on its own, seems unlikely to
911 explain the abrupt nature of the observed field increases in the interior of the anvil.
912 Screening layers on the side of the anvil are unlikely to explain our observations. The
913 abrupt nature of the observed electric field change needs further investigation with
914 modeling studies that include explicit turbulence and mixing and detailed microphysical
915 observations as well as additional observations.

916 The composite measurements from all anvils investigated in ABFM II showed that
917 when the average reflectivity, such as in a 3-km cube, was less than about 5 dBZ, the
918 electric field magnitude was $<3 \text{ kV m}^{-1}$, a value that is highly unlikely to trigger lightning
919 by the Space Shuttle or a similar launch vehicle. Based on this finding, we developed the
920 Volume Averaged Height Integrated Radar Reflectivity (VAHIRR) which combines
921 radar based observations of a volume average reflectivity and the thickness of the anvil.

922 VAHIRR is now being used to increase launch availability in new Lightning Launch
923 Commit Criteria for anvils.

924 The ABFM II measurements showed that the charge structure in these anvils is very
925 complicated with the vertical component of the field often changing polarity during a
926 single aircraft penetration across the anvil. Our ability to investigate and to understand
927 the charge structure was inhibited because we were rarely able to make spiral descents or
928 ascents due to restrictions by Air Traffic Control from the heavy air traffic in Florida.
929 Additional field campaigns in a location in which vertical soundings can be made would
930 be highly desirable.

931 The extensive and detailed measurements of cloud particle concentrations, types
932 and sizes; electric field and coordinated reflectivity obtained during ABFM II provide an
933 excellent data set with which to investigate a number of physical processes in anvils,
934 debris clouds and stratiform regions of Florida thunderstorms. Possible topics include:
935 the charge separation mechanisms and related particle interactions apparently occurring
936 near the melting zone and at higher altitudes in long-lived anvils; changes in particle type
937 (especially riming) during penetrations across an anvil; examination of the charge
938 structure in anvils; the evolution of the particle size distribution by aggregation and
939 sedimentation in both high and weak electric field situations; and the kinematic
940 mechanisms responsible for the updraft and hence enhancement of reflectivity in long-
941 lived anvils. We hope that other investigators might pursue these and/or other topics
942 using the ABFM II data set. Interested investigators may contact Frank Merceret at the
943 Kennedy Space Center Weather Office (francis.j.merceret@nasa.gov) for access to the
944 data.

945

945 ACKNOWLEDGEMENTS

946 We gratefully acknowledge financial support from the National Aeronautics and
947 Space Administration and the National Reconnaissance Office, as well as the advocacy
948 and administrative support of John Madura of the Kennedy Space Center Weather Office.
949 In addition, we would like to acknowledge flight support from. Mike Poellot and the
950 Citation pilots and ground crews; weather support from the 45th Weather Squadron; and
951 ground support from the 45th Space Wing and NASA Kennedy Space Center. We
952 particularly wish to recognize Dr. Harry C. Koons for his extremum analysis of the
953 ABFM II anvil data set and for his thorough and careful contributions. Don
954 MacGorman's comments helped improved the manuscript. The National Center for
955 Atmospheric Research is partially supported by the National Science Foundation.
956

956 REFERENCES

957

958 Bailey, M. and J. Hallett 2002, Nucleation effects on the habit of vapour grown ice
959 crystals from -18 °C To - 42 °C, *Q. J. Royal. Met. Soc.*, **128**, 1461-1484.

960

961 M.G. Bateman, D.M. Mach, S. Lewis, J.E. Dye, E. Defer, C.A. Grainger, P.T. Willis, F.J.
962 Merceret, D. Boccippio, and H.J. Christian, 2005, Comparison of in-situ electric field and
963 radar derived parameters for stratiform clouds in Central Florida, Conf. on Meteorol.
964 Apps. of Lightning Data, AMS Annual Meeting, San Diego, Jan. 23-28, Paper No. P1.10.

965

966 Bateman, M.G., M.F. Stewart, R.J. Blakeslee, S.J. Podgorny, H.J. Christian, D.M. Mach,
967 J.C. Bailey, D. Daskar and A.K. Blair, 2006, A low noise, computer-controlled, internally
968 digitizing rotating-vane electric field mill for airborne platforms, accepted for publication
969 in *J. Atmos. Ocean. Tech.*

970

971 Blakeslee, R.J., H.J. Christian, and B. Vonnegut, 1989, Electrical measurements over
972 thunderstorms, *J. Geophys. Res.*, **94**, 135-140.

973

974 Boccippio, D.J., S. Heckman, and S.J. Goodman, 2000a, A diagnostic analysis of the
975 Kennedy Space Center LDAR network: 1. Data Characteristics, *J. Geophys. Res.*, **106**,
976 4787-4796.

977

978 Boccippio, D.J., S. Heckman, and S.J. Goodman, 2000b, A diagnostic analysis of the
979 Kennedy Space Center LDAR network: 2. Cross sensor studies, *J. Geophys. Res.*, **106**,
980 4769-4786.

981

982 Boyd, B.F., W.P. Roeder, D.L. Hajek, M.B. Wilson, 2005, Installation, upgrade and
983 evaluation of a short baseline cloud-to-ground lightning surveillance system used to
984 support space launch operations, Conf. on Meteorol. Applic. of Lightning Data, Amer.
985 Meteorol. Soc. Annual Meeting, San Diego CA, Jan. 9 – 13,

986

987 Byrne, G.J., A.A. Few, and M.F. Stewart, 1989, Electric field measurements within a
988 severe thunderstorm anvil, *J. Geophys. Res.*, **94**, 6297-6307.

989

990 Cummins, K. L., M. J. Murphy, E. A. Bardo, W. L. Hiscox, R. B. Pyle, and A. E. Pifer,
991 1998, A combined TOA/MDF technology upgrade of the U.S. National Lightning
992 Detection Network, *J. Geophys. Res.*, **103**, 9035– 9044.

993

994 Dye, J. E., J. J. Jones, W. P. Winn, T. A. Cerni, B. Gardiner, D. Lamb, R. L. Pitter, J.
995 Hallett, and C. P. R. Saunders, 1986, Early electrification and precipitation development
996 in a small, isolated Montana cumulonimbus, *J. Geophys. Res.*, **91**, 1231 -1247.

997

998 Dye, J.E., S. Lewis, M.G. Bateman, D.M. Mach, F.J. Merceret, J.G. Ward and C.A.
999 Grainger, 2004, Final Report on the Airborne Field Mill Project (ABFM) 2000-2001
1000 Field Campaign, NASA/TM-2004-211534, National Aeronautics and Space

1001 Administration, Kennedy Space Center, FL, 132 pp. Available from NASA Center for
1002 AeroSpace Information (CASI), 7121 Standard Drive, Hanover, MD 21076-1320.
1003
1004 Dye, J.E. and J.C. Willett, 2006, The enhancement of reflectivity and electric field in
1005 long-live Florida anvils. Submitted to *Month. Weath. Rev.*, Aug.31, 2006.
1006
1007 Field, P.R., Wood, R., Brown, P.R.A., Kaye, P.H., Hirst, E., Greenaway, R., Smith, J.A.,
1008 2003, Ice particle interarrival times measured with a fast FSSP, *J. Atmos. Ocean Tech.*,
1009 **20**, 249-261.
1010
1011 Field P.R., Heymsfield A.J. Bansemer A., 2006, Shattering and particle interarrival times
1012 measured by optical array probes in ice clouds. *J. Atmos. Ocean Tech.*, **23**, in press.
1013
1014 Heymsfield, A.J., and L.M. Milosevich, 1989, Evaluation of liquid water measuring
1015 instruments during FIRE, *J. Atmos. Ocean. Tech.*, **6**, 378-388.
1016
1017 Jayaratne, E.R., C.P.R. Saunders, and J. Hallett, 1983: Laboratory studies of the charging
1018 of soft-hail during ice crystal interactions. *Quart. J. R. Meteor. Soc.*, **109**, 609-630.
1019
1020 Klett, J.D., 1972, Charge screening layers around electrified clouds, *J. Geophys. Res.*, **77**,
1021 3187-3195.
1022

1023 Krider, E.P., H.C. Koons, R.L. Walterschied, W.D. Rust, and J.C. Willett, 1999, Natural
1024 and triggered lightning launch commit criteria (LCC), Aerospace Report No. TR-
1025 99(1413)-1, The Aerospace Corporation, El Segundo, CA, 15 pp.

1026

1027 Lawson, P.R., B.A. Baker, C.G. Schmitt, T.L. Jensen, 2001. An overview of
1028 microphysical properties of Arctic clouds observed in May and July 1998 during FIRE
1029 ACE, *J. Geophys. Res.*, **106**, 14989-15014.

1030

1031 Lawson, R. P., R. E. Stewart and L. J. Angus, 1998, Observations and numerical
1032 simulations of the origin and development of very large snowflakes, *J. Atmos. Sciences*,
1033 **55**, 3209-3229.

1034

1035 Lennon, C and L.S. Maier, 1991, Lightning mapping system, *Proc. Internat. Aerosp. and*
1036 *Grnd Conf. On Lightning and Static Electr.*, Cocoa Beach, FL, Apr. 16-19, 1991, 89-91.

1037

1038 MacGorman, D. R., and W. D. Rust, 1998, *The Electrical Nature of Storms*, Oxford
1039 Univ. Press, New York, 422 pp.

1040

1041 Mach, D. M. and W. J. Koshak, 2003, General matrix inversion technique for the
1042 calibration of electric field sensor arrays on aircraft platforms, *Proc. 12th Internat. Conf.*
1043 *on Atmosph. Electr.*, Versailles, France, 9-13 June, 207-210.

1044

1045 Maier, M.W. , 1991, Evaluation of 1990 bias error corrections for the ESMC cloud-to-
1046 ground lightning surveillance system, CSR-322-003, Eastern Space and Missile Center
1047 Report under Contract F08606-88-C-0014, Computer Sciences, Raytheon Corporation.
1048

1049 Marshall, T.C., W.D. Rust, and W.P. Winn, 1984, Screening layers at the surface of
1050 thunderstorm anvils, Proc. VII Intern. Conf. on Atmosph. Electr., Albany, NY, June 3-8,
1051 pp.346-347.
1052

1053 Merceret, F.J., J.G. Ward, D.M. Mach, M.G. Bateman and J.E. Dye, 2006, On the
1054 magnitude of the electric field near thunderstorm-associated clouds, to be submitted to J.
1055 Appl. Meteorol.
1056

1057 Mohr, C.G., L.J. Miller, R.L. Vaughan, and H.W. Frank, 1986, The merger of mesoscale
1058 data sets into a common Cartesian format for efficient and systematic analysis, *J. Atmos.*
1059 *Oceanic Tech.*, **3**, 143-161.
1060

1061 Office of the Federal Coordinator for Meteorology (OFCM), 2003, *Federal*
1062 *Meteorological Handbook No. 11: Doppler Radar Observations*, part A, 34 pp.
1063

1064 Reiss, R.-D., and M. Thomas, 2001, *Statistical Analysis of Extreme Values*, 2nd Edition,
1065 Birkhauser Verlag, Boston, 443 pp.
1066

1067 Schild, J.J., 2003, Liquid water in thunderstorm anvils over Kennedy Space Center,
1068 Florida during the summer 2001 ABFM field campaign, M.S. Thesis, Univ. of North
1069 Dakota, 55pp.
1070
1071 Strapp, J.W., F. Albers, A. Reuter, A.V. Korolev, U. Maixner, E. Rashke, and Z.
1072 Vukovic, 2001, Laboratory measurements of the response of a PMS OAP-2DC, *J. Atmos*
1073 *Ocean. Tech*, **18**, 1150-1170.
1074
1075 Vonnegut, B., C.B. Moore, R.P.Espinola, and H.H.Blau Jr., 1966, Electric potential
1076 gradients above thunderstorms, *J. Atmos. Sci.*, **23**, 764-770.
1077
1078 Ward, J.L., F.J. Merceret and C.A. Grainger, 2003, An automated cloud-edge detection
1079 algorithm using cloud physics and radar data, NASA Technical Memorandum
1080 NASA/TM-2003-211189, June 2003, 20 pp.
1081
1082 Wheeler, M.W., 1997, Report on the Radar/PIREP Cloud Top Discrepancy Study, NASA
1083 Kennedy Space Center FL, Contractor Report CR-204381, 18 pp.
1084
1085 Willett, J.C., D.A. Davis, and P. Laroche, 1999, An experimental study of positive
1086 leaders initiating rocket-triggered lightning, *Atmospheric Research*, **51**, 189-219.
1087

- 1088 Willett, J.C. and J.E. Dye, 2003, A simple model to estimate electrical decay times in
1089 anvils, *Proc. 12th Intern. Conf. on Atmosph. Electr.*, Versailles, France, June 2003, 267-
1090 271.
1091
1092 Winn, W.P., C.B. Moore, C.R. Holmes, and L.G. Byerley, 1978, Thunderstorm on July
1093 16, 1975 over Langmuir Laboratory: A case study, *J. Geophys. Res.*, **83**, 3079-3092.